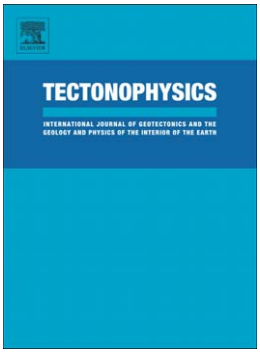

Crystallographic preferred orientations of exhumed subduction channel rocks from the Eclogite Zone of the Tauern Window (Eastern Alps, Austria), and implications on rock elastic anisotropies at great depths

Ruth Keppler, Klaus Ullemeyer, Jan H. Behrmann, Michael Stipp, Robert M. Kurzawski, Tomas Lokajíček

PII: S0040-1951(15)00089-X
DOI: doi: 10.1016/j.tecto.2015.02.011
Reference: TECTO 126550

To appear in: *Tectonophysics*

Received date: 14 October 2014
Revised date: 25 January 2015
Accepted date: 15 February 2015

Please cite this article as: Keppler, Ruth, Ullemeyer, Klaus, Behrmann, Jan H., Stipp, Michael, Kurzawski, Robert M., Lokajíček, Tomas, Crystallographic preferred orientations of exhumed subduction channel rocks from the Eclogite Zone of the Tauern Window (Eastern Alps, Austria), and implications on rock elastic anisotropies at great depths, *Tectonophysics* (2015), doi: 10.1016/j.tecto.2015.02.011

Crystallographic preferred orientations of exhumed subduction channel rocks from the Eclogite Zone of the Tauern Window (Eastern Alps, Austria), and implications on rock elastic anisotropies at great depths

Ruth Keppler (1), Klaus Ullemeyer (1), Jan H. Behrmann (2), Michael Stipp (2), Robert M. Kurzawski (2), Tomas Lokajíček (3)

(1) Department of Geosciences, University of Kiel, Otto-Hahn-Platz 1, D-24118 Kiel

(2) GEOMAR Helmholtz Centre for Ocean Research, Wischhofstr. 1-3, D-24148 Kiel

(3) Institute of Geology ASCR, Rozvojova 269, CZ-165 00 Praha 6

Crystallographic preferred orientations (CPO) of rocks from an exhumed subduction channel of the Alpine orogen were determined using time-of-flight neutron diffraction. This method allows the investigation of large polymineralic samples and, more importantly, the application of full pattern fit methods to constrain CPOs of mineralogically complex rocks. Samples studied include intensely deformed fresh and retrogressed eclogites, as well as metasediments, which are interleaved with the eclogites in the subduction channel. From the CPO, seismic properties of the samples were calculated. *P*- wave anisotropies of the eclogite samples are fairly low, with an average of about 1.5%, and mainly constrained by pronounced omphacite CPO. Growth and deformation of retrograde amphibole in the eclogites also led to a pronounced CPO, which has a large impact on seismic anisotropies by raising them to up to 3.7% and changing the orientations of velocity maxima. Elastic anisotropies of the subducted metasediments are higher (up to 7.4%) and constrained by quartz and mica CPO in clastics and by calcite CPO in marble. V_P/V_S ratios may help to distinguish fresh eclogites from retrogressed ones, and both rock types from mantle peridotites of downgoing lithospheric slabs in seismic imaging. Our data also indicate that subducted terrigenous sediments are not only strongly anisotropic, but also have low V_P/V_S ratios. This way there may be potential to image them by seismic tomography at depth in active subduction channels.

1. Introduction

The interface of convergent plate boundaries is a highly dynamic tectonic environment, featuring deep subduction, offscraping of lower plate materials, underplating, and eventual exhumation by return flow towards the Earth´s surface. The general concept is that of rocks moving in a subduction channel, first established by Shreve and Cloos (1986) and Cloos and Shreve (1988). These authors mainly describe the movement of material to and from depths of 30 km. More recent subduction channel models include the exhumation of previously subducted oceanic crust and sedimentary cover from depths of over 70 km (e.g. Angiboust et al., 2009; Agard et al., 2009). The generally

invoked driving mechanisms are buoyancy of surrounding low-density rocks (e.g. Guillot et al., 2001; Kurz and Froitzheim, 2002), external forcing by continental fragments entering the subduction zone (e.g. De Franco et al., 2008), slab breakoff (e.g. Ratschbacher et al., 2004), or the changeover to an extensional regime in the overriding plate (e.g. Platt, 1986; Behrmann and Ratschbacher, 1989). There is a large number of recent regional studies of exhumed subduction channel rocks, which yield information on their petrology and tectonic history. Examples are the Franciscan Complex of California (e.g. Anczkiewicz et al., 2004), the Mesohellenic subduction zone in the Cyclades (e.g. Schmaedicke and Will, 2003), the Western (e.g. Bousquet, 2008) and the Eastern Alps (e.g. Kurz et al., 1998). Common to all these subduction zones are the thickness of only a few kms, and their lithologies comprising metabasic lenses of variable size embedded in a matrix of lower-density metasediments or serpentinites.

Despite detailed field investigations and numerous models for subduction channels, the exact processes taking place within are far from being completely understood. High resolution seismic imaging – a promising tool for the deconvolution of small-scale structures at depth – is still hampered by inadequate knowledge regarding the velocity structure and elastic anisotropies. Elastic anisotropy data of rocks incorporated in subduction zones are an important source of information for the interpretation of (high resolution) seismic sections, and have been used to aid the understanding of mantle dynamics (e.g. Montagner and Tanimoto, 1990; Silver, 1996; Montagner and Guillot, 2003). In this context crystallographic preferred orientation (CPO) of the rock constituents can be used as a powerful tool to predict the elastic anisotropy of deformed subduction channel rocks. However, the acquisition of CPO data and, thus, obtaining first-hand information on elastic anisotropies of polymineralic rocks is not straightforward. Most studies on polymineralic rocks were conducted on materials from the upper and lower crust (e.g. Ivankina et al., 2005; Kitamura, 2006; Ullemeyer et al., 2006), or on rocks originating from above and below the continental Moho (e.g. Barruol and Kern, 1996; Pros et al., 2003; Ullemeyer et al. 2010; Llana-Fúnez and Brown, 2012). Elastic data for subduction channel rocks were provided by Mauler et al. (2000), Bascou et al. (2001), and Worthington et al. (2013), who investigated mineral CPOs of eclogites using EBSD (electron backscatter diffraction) and bulk rock elastic anisotropies calculated from the CPO data. However, these studies neither include metasedimentary rocks in the subduction channel nor retrogressed eclogites, which yield information on the processes and changes in state during exhumation. Furthermore, a methodical drawback of EBSD is the poor grain statistics due to limited sample size, which has consequences when calculating rock physical properties from CPO data.

To overcome these methodical limitations, and to offer a more comprehensive insight into the petrophysics of rock associations in a subduction channel, we present CPOs and bulk rock elastic anisotropies of principal rocks from an exhumed subduction channel: the Eclogite Zone (EZ in the

following) of the Tauern Window in the Eastern Alps. The CPOs were acquired from time-of-flight neutron diffraction spectra applying full pattern fit method for the texture evaluation, which permits a fully quantitative investigation of large rock samples with complex mineralogy. From the CPO data, we have modeled elastic anisotropies. In addition, two eclogite samples were the subject of direct *P*-wave velocity measurements on spherical samples, giving an impression of the crack influence on the elastic rock properties at shallow and intermediate crustal depths. Our results allow to make inferences regarding the seismic attributes of subduction channels, especially acoustic anisotropy, and guide future visualization of subduction channel structure and physical properties.

2. Geological overview of study area

The EZ is located at the southern margin of the Tauern Window in the Eastern Alpine Orogen (Figs. 1A and 1B). The Tauern Window is a tectonic window exposing basement and cover of the lower European plate, as well as Penninic oceanic units that were initially subducted beneath the Adriatic plate and subsequently incorporated in the Alpine stack of tectonic nappes during continental collision in the Tertiary. The EZ is considered to represent the ocean-continent boundary at the distal European margin. Its general character is a volcano-sedimentary sequence formed during Jurassic rifting of the Penninic ocean (Kurz et al., 1998). Driven by the negative buoyancy of the downgoing Penninic oceanic slab, the EZ entered the subduction channel in the course of Adria-Eurasia convergent movements. The rocks were subjected to PT conditions of 2.0-2.5 GPa and 600 +/- 30°C (Dachs, 1990, Stöckert et al., 1997; Hoschek, 2001; 2004). Rb-Sr dating by Glodny et al. (2005) and Lu-Hf dating by Nagel et al. (2013) indicate an Oligocene age for the peak PT conditions, and a fast exhumation thereafter within 1-2 Ma. Because of the fast exhumation from great depths, only part of the rocks suite was severely affected by retrograde metamorphism. With large coherent sheets of eclogite and interleaved metasediments preserved, the area offers the opportunity to study the effects of retrogression along intensity gradients in the field, and make predictions about the changes in petrophysical behavior as rocks are being progressively exhumed.
Currently , the EZ is sandwiched in between European continental units to the north (Venediger nappe) and Penninic oceanic units to the south (Glockner nappe), and is dipping steeply to the SSE (Figs. 1 C and 2). The EZ comprises eclogite lenses of various size, surrounded by a matrix of gneisses, micaschists, quartzites, marbles and metaconglomerates (Fig. 2).

3. Methods

CPO measurements were performed at the neutron time-of-flight (TOF) texture diffractometer SKAT at the Frank Laboratory of Neutron Physics at JINR, Dubna, Russia (Ullemeyer et al., 1998; Keppler et al., 2014). The high penetration capability of neutrons in matter together with the large beam cross section of the SKAT (50 x 95 mm^2) allow the application of large-volume samples in the neutron experiment, e.g. of spherical samples with volumes of about 65 cm^3. This is an important prerequisite, because the investigated samples are usually coarse-grained. Moreover, since complete diffraction patterns are recorded in a TOF experiment, highly sophisticated methods like the so-called 'Rietveld Texture Analysis' (RTA) can be used for the texture evaluation, allowing the simultaneous determination of all mineral textures even for samples with complex mineralogy (Von Dreele, 1997; Matthies et al. 1997). We used the MAUD software for the texture evaluation (Lutterotti et al., 1997; Wenk et al., 2010), for the discussion of practical limitations refer to Wenk et al. (2012) and Keppler et al. (2014). Since RTA requires knowledge of the mineral structures present in the sample, mineral assemblages and chemical compositions were determined by means of microprobe analysis on a JEOL JXA 8200 Electron microprobe.

From the CPOs of the main rock constituents and particular single crystal elastic constants and volume fractions the elastic moduli of bulk rock were calculated by using the Christoffel equation (e.g. Christoffel, 1877; Mainprice and Humbert, 1994),

$$Det\left|\Gamma_{ij} - V^2\delta_{ij}\right| = 0, \quad (1)$$

where V – the phase velocity of the P- , S_1 or S_2 waves, δ_{ij} – the Kronecker delta, Γ_{ij} – the Christoffel tensor,

$$\Gamma_{ij} = a_{ijkl}x_k x_l. \quad (2)$$

Parameters a_{ijkl} represent the density-corrected elastic (stiffness) moduli, $x_k x_l$ are the direction cosines of the wave propagation direction. Hill (1952) has shown that the widely used Voigt (1928) and Reuss (1929) averaging schemes deliver upper and lower bounds of the elastic moduli, respectively. Other averaging schemes were proposed (e.g. Matthies and Humbert, 1995; Matthies, 2011), however, the true values of parameters a_{ijkl} are still somewhat uncertain. Therefore, we decided to use the most straightforward approach by consistently applying the Voigt averaging scheme, and at the same time keeping in mind that the recalculated velocities obtained are maximum velocities. The single crystal elastic constants were taken from the literature (omphacite: Bhagat et al., 1992; garnet: Babuska et al., 1978; hornblende: Aleksandrov and Ryzhova, 1961; glaucophane: Bezacier et al., 2010; muscovite: Vaughan and Guggenheim, 1986; quartz: Heyliger et

al., 2003; albite: Brown et al., 2006; epidote/zoisite/clinozoisite: Aleksandrov et al., 1974; calcite: Dandekar, 1968). Whereas the elastic constants of quartz, muscovite and albite are confirmed to be reliable, the elastic constants of some other minerals are at least questionable. This holds in particular true for hornblende, the main constituent of the amphibolite TW32 (see Table 1). Microprobe analyses revealed glaucophane as the amphibole phase in most samples. Its chemical formula shows differences compared to the glaucophane individual of Bezacier et al. (2010), but the elastic data of Bezacier et al. (2010) are the only available and we were forced to use them. The omphacite composition varies from $Di_{65}Jd_{35}$ to $Di_{45}Jd_{55}$, Bhagat et al. (1992) report $Di_{38}Jd_{62}$ for their sample. The composition of garnet is close to the almandine end member in the pyrope-almandine-spessartine system, which justifies the use of the almandine elastic constants of Babuska et al. (1978). Nevertheless, we conclude that for some main rock constituents the elastic constants may differ from the 'true' mineral constants in our samples. Elastic data of chlorite, not present in excess of 5 percent in any of the samples, were approximated by the muscovite elastic constants. In this case and for other minerals like epidote/zoisite/clinozoisite contents in the samples studied are lower than the 10 percent threshold that would make the CPO of a particular mineral relevant for the physical properties (see Mainprice and Ildefonse, 2009).In Fig. 3, *P*- wave velocity distributions and particular *P*- wave anisotropies are given for the main rock constituents.

Many experiments have shown that the elastic properties of rocks at small confining pressures are largely controlled by the crack fabric (e.g. Kern et al., 2002; Pros et al., 2003; Ivankina et al., 2005; Ullemeyer et al., 2006; Kern et al., 2008). The unique experiments of Christensen (1974) on mantle rocks confirmed crack influence to pressures of about 1 GPa, and there is evidence from low-pressure measurements that crack influence up to 1 GPa (or more) is valid for other rock types as well (Ullemeyer et al., 2011). We, therefore, accept that our texture-based predictions of the elastic constants are valid for great depths only. Nonetheless, in order to get an impression on the crack influence at smaller depths, complete *P*- wave velocity distributions were determined on an amphibolite and an eclogite sample applying the pressure apparatus of the Institute of Geology ASCR, Prague, Czech Republic (Pros et al., 1998). The measurements were performed at various pressure levels starting at ambient conditions (0.1 MPa), the maximum pressures achieved in the experiments (300 and 400 MPa, respectively) are sufficient to close most open microcracks, allowing in particular the judgement of anisotropy differences to the crack-free medium.

In order to help quantification of the effects of retrogression on the elastics properties of the eclogite samples, bulk chemical compositions of the retrogressed eclogite samples RK4 and RK20 were used to model the pristine equilibrium mineral assemblages and modal mineral amounts at peak metamorphic conditions of 600-630 °C and 2.0-2.5 GPa (Stöckhert et al., 1997; Hoschek, 2001; 2004). For this purpose the thermodynamic modeling tool THERIAK/DOMINO is used (de Capitani and

Brown, 1987; de Capitani and Petrakakis, 2010). The equilibrium assemblage was calculated utilizing a modified Holland & Powell database. To avoid interferences of different implemented amphibole solid solution models, only the two-endmember glaucophane model was applied. Such an adjustment is reasonable as only the relevant high-pressure realm is considered, and therefore only blueschist facies amphiboles are expected. Bulk compositions of the rocks were calculated from averaged microprobe mineral analyses, and corresponding modal amounts were taken from RTA. All calculations were carried out assuming excess of a hydrous fluid. In order to reproduce the exact amount of carbonates present in the rock sample in the retrogressed state, a stoichiometric quantity of CO_2 was added to the fluid composition of sample RK4. Comparison of the retrogressed and peak-grade mineral compositions allow to assess the likely change in elastic properties and anisotropy associated with retrogressive changes during the exhumation stage.

4. Compositions and microfabrics of the samples studied

The composition of the eclogites is quite variable. Main constituents are omphacite and garnet, changing amounts of glaucophane, barroisitic hornblende, clinozoisite, quartz, phengite, paragonite, albite and minor amounts of dolomite, calcite, kyanite and rutile (Table 1). The mesoscopic and microscopic fabric of the eclogites is also highly variable (Fig. 4). There are coarse-grained and fine-grained varieties with random mineral distribution (RK3, RK20), as well as fine grained and strongly foliated eclogites displaying compositional layering (RK1, RK4, RK49, MS112, TW33). Elongated omphacite grains define a clear lineation on the foliation plane. In mylonitic eclogites the omphacite forms aggregates of small recrystallized grains. Garnet exhibits prograde zoning and either occurs in layers or as randomly distributed cluster. Layered samples show garnet- and quartz- rich layers alternating with omphacite- rich layers of variable thickness (Fig. 4). In samples containing zoisite and dolomite, both these phases are often concentrated in distinct layers. Small and dispersed zoisite grains within omphacite- rich layers are aligned parallel to the foliation, whereas in zoisite- rich layers the grains are larger and do not show shape preferred orientation (SPO) (see RK1 in Fig. 4). Quartz grains do not exhibit SPO. In the eclogites phengitic mica (Si: 3.26-3.37) is always aligned parallel to the foliation, whereas paragonite is randomly oriented.

The metasediments investigated in this study comprise gneisses, micaschists, mica- bearing quartzites and marbles. Particular modal compositions are summarized in Table 1. The clastic metasediments exhibit a strong foliation defined by mica (Fig. 5). The phengite component of the micas is lower than in the eclogite samples (Si: 3.07-3.24). Most of the clastic metasediments contain minor amounts of clinozoisite, and the gneisses contain feldspar. The only marble sample is mainly composed of medium-grained calcite and shows a weak foliation.

5. Results

5.1. Crystallographic preferred orientations

5.1.1. Eclogites

All eclogites exhibit a distinct CPO of omphacite. Position and intensity of the pole density maxima are variable, however, (001) always displays a maximum parallel to the stretching lineation (Figs. 6 and 7). In some samples (RK1, RK3, TW33) the maximum is cluster-like, in others, (001) forms a more or less pronounced girdle within the foliation plane (RK4, RK20, RK49, MS112). (010) is mostly concentrated normal to the foliation plane, but can also be distributed in a girdle perpendicular to the lineation.

Glaucophane also displays pronounced CPO in all retrogressed eclogites (Fig. 6). As in the case of omphacite the glaucophane CPOs are variable. Glaucophane (001) mostly parallels the omphacite (001) lattice plane, however, one sample shows clear deviation from this rule, an angular deviation of about 40° within the foliation plane is valid (sample RK20, Fig. 6). Glaucophane (100) always has the maximum pole density normal to the foliation plane. The barroisitic hornblende in sample RK4 shows girdle-like distributions of the (100) and (001) lattice planes, the latter scattering within the foliation plane. The (100) girdle is very weak and oriented perpendicular to the kinematic Z axis (Fig. 6). In this sample, there is also a pronounced (010) maximum normal to the foliation (not depicted).

With the exception of sample RK4, the phengite (006) basal planes have strong axial symmetric maxima parallel to the foliation normal. If paragonite is present in significant amounts, (006) exhibits only weak preferred orientation, but the maximum pole density also parallels the foliation normal (sample RK3, Fig. 6). Garnet, the acoustically isotropic major constituent of the eclogites, has nearly random distribution, as exemplified by two garnet pole figures of samples TW33 and MS112 (Fig. 7).

The zoisite CPO of sample RK1 is of intermediate strength with (010) parallel to the lineation and a slight tendency of (100) to form a girdle around the lineation (Fig. 7). Calcite, dolomite and albite, if present, always display very weak preferred orientations close to a random distribution (for this reason not presented).

Despite the generally low volume fraction, quartz has a weak but well-defined CPO, as exemplified by sample MS 11.2 bearing 15% quartz (Table 1). The (003) lattice plane displays a small circle distributions around the foliation normal. The (011) and (101) lattice planes have intensity clusters parallel to the foliation normal, whereas (011) exhibits additional scattering in the foliation plane

(Fig. 7). The overall layout corresponds to a nearly perfect axial symmetric texture with the foliation normal as the symmetry axis.

5.1.2. Metasediments

In the metasediments, the quartz CPO is more pronounced compared to the eclogites. The maximum pole densities are in the order of 2.0 [m.r.d.], except for the c- axis distribution of sample RK6, which is two times higher (Fig. 8). Mostly, asymmetric c- axis crossed girdles or point maxima slightly inclined to the foliation normal are observed, sample RK6 exhibits an additional c- axis maximum close to the center of the pole figure. The (110) maxima are always close to the margin of the pole figures, in agreement with the inclination of the c- axis, they are inclined with respect to the stretching lineation (Fig. 8). The (100) lattice planes show pole density distributions in agreement with the geometrical relationship of the quartz lattice planes. Their outline is either similar to the (110) pole figure (sample RK6), or dissimilar (sample RK5). The (011) and (101) rhombs generally have weak preferred orientation, with maximum pole densities either within the foliation plane (RK5), on small circle girdles around the foliation pole (RK6 and RK28), or normal to the foliation ((101) pole density maximum of sample RK28). If present, albite has a random CPO (not presented). The (006) basal planes muscovite/phengite exhibit very strong maxima normal to the foliation (Fig. 8) with much higher pole densities compared to the eclogites (Figs. 6 and 7).
The calcite CPO of the marble sample RK17 is of intermediate strength. The (110) lattice planes form a girdle within the foliation plane, the maximum pole density on the girdle parallels the stretching lineation. The (006) lattice planes make a maximum parallel to the foliation normal. The general layout of the calcite CPO is axial symmetric with the foliation normal as the symmetry axis.

5.2. *P*- wave anisotropy

5.2.1. Eclogites and retrogressed counterparts

P- wave velocities (V_P) of the eclogite samples calculated from the CPOs vary between 7.45 and 8.10 km/s (Fig. 9). *P*- wave anisotropies of the eclogite samples are mostly low, with the highest value (3.7%) for the retrogressed sample RK20, and the lowest one (0.4%) for the non-retrogressed sample RK1, which has a high Zoisite content (see Table 2). In all samples, the velocity maxima are close to the omphacite (001) pole density maximum, and, if present, the amphibole (001) pole density maximum. In Sample RK20, where the pole density maxima of the two minerals exhibit an angle of about 40° within the foliation plane, the calculated velocity maximum lies between both these

maxima. Lowest *P*- wave velocities are normal to the foliation throughout, i.e., high velocities are always located within the foliation plane. *S*- wave velocities in the eclogites vary between 4.82 and 4.23 km/s (V_{S1}), and between 4.81 and 4.22 km/s (V_{S2}) (Table 2). We avoided graphical representation of the *S*- wave velocity distributions, because the velocity differences are mostly some tenths of meters (see Table 2) and, therefore, insignificant.

P- wave velocity distributions of samples RK4 and RK20 were also calculated for the high-pressure mineral assemblages obtained from thermodynamic modeling by means of the THERIAK/DOMINO tool (RK4HP and RK20HP in particular figures and tables). The most prominent difference to the actual composition obtained from RTA is the absence of amphibole minerals (Table 1). Figure 10 shows an equilibrium assemblage diagram illustrating the high pressure assemblage of sample RK20, the frame in the diagram indicates the PT conditions of the EZ we used for modeling. *P*- wave velocities recalculated for the modeled samples are higher (RK4HP) or lower (RK20HP) compared to the retrogressed counterparts. Judging the isotropic mean V_{Piso}, the velocity increase of sample RK4HP is approx. 0.7 km/s, the decrease of sample RK20HP is much less (approx. 0.2 km/s, Table 2). In both cases, however, *P*- wave anisotropy decreases. The already weak anisotropy of the strongly retrogressed eclogite RK4 is reduced even more and becomes insignificantly small (< 1%), in case of the less retrogressed eclogite RK20 anisotropy still exceeds 2%, although the decrease is remarkable (compare magnitudes in Table 2).

The experimental *P*- wave velocity distributions determined at moderate confining pressures of 300 MPa (amphibolite sample TW32) and 400 MPa (eclogite sample TW33) show different relationships to the crack-free (CPO-derived) counterparts. The amphibolite (TW32) has a slightly higher 'experimental' velocity level in the order of 0.1 km/s (Table 2). Since the experimental velocities should not exceed the CPO-derived ones, this is a clear indicator that the bulk error introduced by applied methods (uncertainties of the CPO estimates, inaccurate mineral elastic constants, experimental errors etc.) is 0.1 km/s to the best. Judging the velocity vs. pressure trends of the minimum and maximum velocities (Fig. 9B), further velocity increase with increasing pressure and, accordingly, a still higher error level can be implied from the trends. Whether, despite these peculiarities, the calculated *P*- wave anisotropies are realistic will be the subject of discussion.

Concerning the eclogite (TW33), the relationships are somewhat different. The calculated velocities exceed the experimental velocities, as expected from theory. From the experimental velocity vs. pressure trends further velocity increase for pressures beyond 400 MPa is difficult to infer (Fig. 9B), but appears to be possible. As for the amphibolite, the 'true' level of the calculated *P*- wave velocities is questionable and should be the subject of discussion.

5.2.2. Metasediments

In the metasediments the calculated *P*- wave velocities are generally lower compared to the eclogites, ranging from 6.24 to 6.86 km/s. *P*- wave anisotropies, on the other hand, are higher and approach 7.4% (Table 2). In the paragneiss sample (RK28) the highest velocities are evenly distributed within the foliation plane and the velocity minimum parallels the foliation normal, i.e., the velocity distribution is more or less axial symmetric (Fig. 9). The micaschist sample (RK5) deviates from axial symmetry, because two velocity maxima at angles of approx. 45° with respect to the lineation are observed (Fig. 9). The micaquartzite (RK6) shows an uncommon relation to the sample reference frame with the velocity maximum apart from the foliation plane and two regions of minimum velocity (Fig. 9). The marble sample has the highest velocity roughly parallel to the lineation with some dispersion in the foliation plane, and the lowest velocity is located normal to the foliation plane.

5.3. V_P/V_S ratios

V_P/V_S ratios of the eclogite samples are between 1.7 and 1.75. They are slightly higher for the retrogressed samples RK4 and TW32 with values of 1.77, and 1.78, respectively (Table 2). In the clastic metasedimentary samples the V_P/V_S values are significantly lower with values between 1.48-1.60. A much higher value of 1.85 was obtained for the marble sample.

6. Discussion

Elastic anisotropy of rocks is, to a large part, constrained by the CPO of its constituent mineral phases, which, in turn, is caused by deformation of the rocks. As Mainprice and Ildefonse (2009) point out, only mineral percentages above 10% play an important role for rock physical properties. In this study, all mineral phases were included into calculation of the elastic anisotropy of bulk rock. Garnet does not exhibit pronounced elastic anisotropy, we, therefore, used the isotropic average of the elastic constants. This might have been possible also in the case of random textures, however, we preferred to average the contribution of particular minerals from the Orientation Distribution Function and the anisotropic mineral elastic coefficients.

The reliability of the predicted elastic anisotropy depends on accuracy of the CPO estimates and mineral elastic constants. A possible source of error is the rock modal composition delivered by RTA. Varying the volume fractions of the rock constituents can lead to the changes of anisotropy. Our observation is that modifications of a few percentages have no effect at all. Accordingly, the error contribution of the minor rock constituents is negligible. If the modification approaches 10%, the

effect becomes visible, in particular for mica minerals exhibiting P- wave anisotropies in the order of 50%. The effect of erroneous CPO estimates in particular of rocks bearing many phases is much harder to assess. Methodical investigations of Keppler et al. (2014) show that, the orientational features of the CPOs of the main rock constituents can be reproduced well, but differences due to texture strength may occur.

6.1 Eclogites

6.1.1. CPO development

The omphacite CPO in the eclogites is variable, exhibiting L- type (lineation dominated), S- type (foliation dominated) or transitional (SL- type) fabrics. The transitional fabrics predominate (Figs. 6 and 7). The CPO geometry has been interpreted as relating to strain geometry (e.g. Kurz and Froitzheim, 2002), with L- type fabrics revealing constrictional strain, S- type fabrics indicating oblate strain, and transitional fabrics suggesting plain strain deformation (e.g. Helmstaedt et al., 1972).
The retrograde glaucophane – a main rock constituent of many eclogites – also exhibits variable CPO. Appearence and CPO development of glaucophane are very likely related to deformation during exhumation. As in the case of omphacite, the strain geometry may have been variable. An important result of the active deformation during exhumation is the degree of retrogression, which is reflected in different glaucophane volume fractions (Table 1). However, in most samples the layout of the glaucophane CPO corresponds to that of omphacite (Fig. 6). This indicates that the CPOs of both minerals formed during rock exhumation, and similar strain geometries persisted in the subduction channel for a long period. The retrogressed eclogite RK20 represents a significant exception, because the orientation of the glaucophane lineation (direction of the pole density maximum of the (001) lattice plane) deviates from the omphacite lineation (Fig. 6). This indicates that the direction of maximum principal extension in this sample changed after formation of the omphacite CPO, but prior or simultaneously to formation of the glaucophane CPO. Passive rotation of the eclogite block as a whole within the surrounding metasediments appears to be the most probable explanation for the rotating stress field. The uncommon barroisite CPO of sample RK4 with a weak girdle tendency of (100) is unusual for amphibole (Zhang et al., 2013).
Albite as a member of the retrograde mineral assemblage formed at a late stage of exhumation. The random CPO suggests that no dislocation creep was active at this stage of exhumation. Other deformation mechanisms cannot be excluded, but, obviously, did not lead to preferred orientation of albite.

In the eclogites, phengitic mica was already present during HP deformation, as confirmed by its high silica content. Strength of the (006) basal plane maximum indicates a well-developed foliation, except for sample RK1, which has a much lower pole density maximum (Fig. 7). The more fluctuating character of the foliation is visible also on hand specimen. If quartz is present, the weak CPO is almost perfectly axial symmetric with the foliation normal as the symmetry axis (Fig 7). Due to the highly ductile behavior of quartz even at low temperatures, oblate strain can be derived from this feature for the very last stages of deformation.

Generally, no correlation between compositional layering and texture strength was observed. Layered samples do not necessarily exhibit a more pronounced CPO than samples with a random grain distribution. Furthermore, no correlation between grain size and the CPO strength of the samples was found. For example strongly layered sample RK1 exhibits much lower texture values in m.r.d. than sample RK3, which exhibits a random mineral distribution (Table 1 and Figs. 4 and 6).

6.1.2. Elastic anisotropies

The CPO- derived elastic anisotropy of the eclogites is mainly constrained by the omphacite CPO and, if present, the amphibole CPO. Phengite contributes significantly if particular volume fractions are large enough. Due to consistent CPO type with the alignment of the basal plane within the foliation, and due to very high single crystal anisotropy (Fig. 3), phengite generally decreases velocity normal to the foliation. The contribution to the velocity level within the foliation is vice versa. Garnet is basically isotropic and does not contribute to anisotropy, due the high isotropic velocity in the order of 9 km/s the contribution to bulk rock velocity can be significant if large volume fractions are present.

The relationship of the kinematically significant lattice planes of omphacite ((010) and (001)) and amphibole ((100) and (001)) to the single crystal *P*- wave distribution is not simple. In case of the omphacite, both the (010) and (001) lattice planes occupy intermediate positions between the directions of minimum and maximum velocity (Fig. 3). The velocity in (010) direction is closer to the minimum velocity and the velocity in (001) direction is closer to the maximum velocity. In case of the amphibole, the orientation differences between (100) / minimum velocity and (001) / maximum velocity are a few degrees only (Fig. 3). Especially in case of omphacite, the *P*- wave velocity distributions are hard to infer directly from the pole figures. However, if the (001) lattice planes of omphacite and amphibole exhibit strong coinciding maxima parallel to the lineation (no dispersion within the foliation plane), the same applies to the velocity distribution (sample RK3 in Figs. 6 and 9). If the omphacite and amphibole (001) lattice planes are dispersed within the foliation plane, the velocity maximum also tends to form a more or less pronounced girdle within the foliation plane

(sample RK49 in Figs. 6 and 9). The strongly retrogressed eclogite RK4 shows clear girdle tendencies of omphacite (001) and hornblende (001), but the velocity distribution exhibits a point maximum parallel to the lineation. The unexpected relationship is caused by the anomalous amphibole CPO with the (100) lattice plane forming a nearly complete – but weak – girdle around the Y axis of the structural reference frame (Figs. 6 and 9). The retrogressed eclogite RK20 with different orientations of the omphacite (001) and amphibole (001) pole density maxima shows a velocity maximum between these maxima (Figs. 6 and 9).

Elastic anisotropy of the eclogites is always small with magnitudes mostly < 2%, except for the retrogressed eclogite RK20 (A = 3.7%), which yields the highest glaucophane volume percentage in the samples (Table 1). Elastic anisotropies of the simulated HP eclogites RK4HP and RK20HP bearing only the high-pressure mineral assemblages are dominated by the omphacite CPO due to the lacking influence of the amphibole CPO. In both cases the overall elastic anisotropy decreases. For sample RK4HP it becomes insignificantly small (0.7%), for sample RK20HP it markedly goes down to 2.3% (RK20: 3.7%, Table 2). This shows that the retrograde metamorphic overprint of eclogites during exhumation is capable of increasing elastic anisotropy due to the formation of amphibole, provided there is a CPO-forming mechanism during exhumation.

6.2 Metasediments

6.2.1. CPO development

The asymmetric crossed girdles of quartz (003) of samples RK5 and RK28 (Fig. 8) are indicative of non-coaxial shear with combined basal <a>, prism <a> and rhomb <a> slip (e.g. Schmid and Casey, 1986). Sample RK6 exhibits a strong quartz (003) maximum at the border of the pole figure. The inclination with respect to the foliation normal indicates non-coaxial shear (Fig. 8). A weaker maximum in the foliation plane points to additional prism <a> slip. Hence, basal <a> slip is the predominant slip system (Schmid and Casey, 1986; Stipp et al., 2002). The quartz textures and observed quartz recrystallization microstructures are characteristic of dislocation creep in the metasediments of the Eclogite Zone. The asymmetry of the CPO is missing in the eclogites (see also Behrmann and Ratschbacher, 1989), i.e., non-coaxial shearing within the subduction channel mainly affected the clastic metasediments surrounding the eclogite bodies. In all clastic metasediments, the mica always shows pronounced basal plane alignment parallel to the foliation plane (Fig. 8). The high phengite component of mica indicates high pressure metamorphism of the metasediments. Since the orientation of the main foliation of the metasediments resembles the orientation in the eclogite

bodies, it is likely that deformation concordantly affected both rock associations, as already assumed by Behrmann and Ratschbacher (1989).

The calcite CPO of the marble RK17 is weak and has a clear axial symmetry of all lattice planes with the foliation normal as symmetry axis indicating pure shear deformation. Slight maxima on the girdle distributions apply (see (110) in Fig. 8). This type of CPO is typical for plastically deformed marbles with combined dislocation glide and twinning as CPO forming deformation mechanisms (Wenk et al., 1987).

6.2.2. Elastic anisotropies

In the clastic metasediments, bulk rock *P*- wave velocity distributions are always dominated by the mica and quartz CPOs in dependence on particular volume fractions. The strongly foliated paragneiss RK28 shows clear predominance of the mica due to the very strong preferred orientation of the (006) basal planes (Fig. 8), the high single crystal anisotropy (Fig. 3) and the high volume fraction approaching 19% (Table 1). As the distribution of P-wave velocities with respect to crystallographic direction in muscovite single crystals is almost biaxial, with a very strong anisotropy (see Fig. 3), representation of the basal plane textures (see Fig. 8) is sufficient to understand the textural contribution of mica to the calculated p-wave anisotropies in the metasediments. For a mica-rich mylonite, Behrmann (1984) showed that strong basal plane textures may well be accompanied by weak CPO of other reflections. Such a texture constrains the geometry of Vp anisotropy patterns to be approximately biaxial with a Vp minimum perpendicular to the foliation, as is the case in the micaschist and paragneiss examples in Fig. 9. Due to weak CPO strength (Fig. 8), the contribution of quartz is negligible despite a volume fraction of 50% (Table 1). Albite exhibits random preferred orientation and therefore lowered the overall anisotropy of this sample. In samples RK5 and RK6, quartz has large influence on the modeled elastic anisotropies due to a strong CPO and higher volume fractions (71% and 92%, respectively). The three-fold symmetry of the quartz single crystal velocity distribution (Fig. 3) makes it impossible to directly infer the influence of quartz on bulk rock velocity distributions. In the case of sample RK5 with clear predominance of the mica (very strong CPO and 24 vol%), quartz causes the splitting of the mica-controlled high velocity girdle within the foliation plane into two maxima. In contrast, the effect of the mica (8 vol%) is hardly visible in the case of sample RK6, despite the very strong preferred orientation (Fig. 8). To some extent, the velocity distribution of the monomineralic marble RK17 can be inferred from the CPO. As expected, the direction of minimum velocity parallels the (006) maximum. The position of the velocity maximum parallel to the lineation cannot be directly inferred from the CPO, but the elongation of the maximum within the foliation plane correlates with the axial symmetric layout of the CPO.

Observed anisotropies of the metasediments range from 5.1% to 7.4%. They are considerably higher as for the eclogites (0.4% - 1.8%) and the retrogressed eclogites (1.2% - 3.7%; Table 2). In the case of samples RK5 and RK28, observed magnitudes of 7.4% and 6.8% can be attributed to the high volume fraction of the mica with very strong preferred orientation. The quartz textures are comparably weak and make no significant contribution. Sample RK6 also shows strong preferred orientation of the mica, but the volume fraction of 8% is too small to determine the layout of the velocity distribution and to significantly control anisotropy. The quartz CPO is rather strong compared to other samples (Fig. 8), together with the high volume fraction of quartz (92%) this causes the observed anisotropy magnitude of 5.3%, despite the three-fold symmetry of the single crystal velocity distribution (Fig. 3). Anisotropy of the monomineralic marble RK17 corresponds to expectations from CPO strength and CPO symmetry. It appears that the much higher degree of mica preferred orientation is mainly responsible for the higher anisotropy level in most metasediments. Some eclogites/retrogressed eclogites also bear considerable amounts of mica in the order of 10% – 15% (samples RK1, RK3, RK4), but the very weak degree of preferred orientation (Figs. 6 and 7) prevents significant contribution of the mica to bulk rock anisotropy. The anisotropy level of the essentially monomineralic samples is either controlled by the CPO strength (sample RK6) or by the simple CPO geometry (sample RK17).

6.3 Comparison of modelled and laboratory data

The elastic anisotropy of rocks is largely influenced by the CPO of their constituent minerals. However, other factors like oriented microcracks or an SPO of the mineral grains can further influence elastic properties. Therefore, P-wave velocities of two eclogite samples were additionally measured in the laboratory for a comparison to the modeled data. The experimental and calculated *P*- wave velocity distributions of samples TW32 and TW33 exhibit coinciding maxima and minima, the outlines of the patterns are slightly different (Fig. 9A). Such a principal agreement, which has been observed also by Mauler et al. (2000) and Abalos et al. (2010) indicates that the influence of the crack fabric is mainly due to quantities. The much larger decrease of the experimental minimum velocity compared to the experimental maximum velocity indicates that the influence of microcracks is anisotropic, and that the microcracks essentially parallel the mica basal planes. Differences are due to anisotropy, which is generally higher for the experimental velocity distributions (Table 2). We already described the considerably lower velocity level of the calculated velocity distribution of sample TW32 compared to the experimental one (Fig. 9B). The most probable explanation is that the elastic constants of hornblende used for the averaging do not fit the actual ones. Microprobe analyses revealed that the amphibole composition of this sample does not match the composition of glaucophane as for all other eclogites and retrogressed eclogites. Hence, we used elastic constants of

Aleksandrov and Ryzhova (1961) for the averaging. Compared to glaucophane, the *P*- wave velocities recalculated from the elastic constants are lower (hornblende: 5.98 – 7.86 km/s; glaucophane: 6.30 – 9.27 km/s), and this may explain the surprisingly low velocity level of the calculated *P*- wave distribution. Simply shifting the calculated velocity pattern as a whole to higher velocities would not change anisotropy significantly, so we suppose that the estimated anisotropy magnitude is affected by some error but realistic. In conclusion, the comparison indicates a remarkable anisotropy difference for the eclogite (TW33), at intermediate crustal depths it is approximately three times higher as for the crack-free (CPO- derived) sample. For the retrogressed eclogite (TW32) it is roughly 1.5 times higher. Such raw estimates give an idea about the increasing influence of the crack fabric during exhumation. According to Christensen (1974) the influence of microcracks is nonexistent at pressures exceeding about 1 GPa, which means for rocks in deeper levels of the subduction channel (e.g. more than 30 km), the modeled anisotropies are expected to be realistic.

Measured elastic anisotropies of gneisses and micaschists are likewise higher than those modeled from compositions and CPO (cf. Meltzner and Christensen, 2001; Zappone et al., 2000; Punturo et al., 2005). Generally the discrepancies are larger than in case of the eclogites. Again, this indicates that preferentially oriented mica exerts a strong influence on velocity anisotropy. In samples RK5 and RK6 of this study, the quartz CPO largely controls the modeled elastic anisotropies and not the mica CPO. Because of the effects induced by microcrack fabric the modeled values from this study need to be considered as lower bound estimates. The same is true for the 5.1% anisotropy modelled for the marble sample with a weak CPO (RK17; Table 2), which is at the lower bound for experimentally measured anisotropies of marble (6 - 12 %, depending on the strength of the foliation; Zappone et al., 2000; Punturo et al., 2005).

6.4 V_P/V_S ratios

Calculated V_P/V_S ratios of the fresh eclogite samples are about 1.70-1.75 (Table 2). These values are somewhat lower than those obtained by Kern et al. (1999), or Worthington et al. (2013), who modeled V_P and V_S Laboratory investigations of Gao et al. (2001), on the other hand, produced a wide spread of V_P/V_S ratios between 1.70 and 1.86 for fresh eclogite samples, and values of up to 1.87 for retrogressed samples. Considering the suite of samples in the present study retrogression of eclogite, ultimately leading to amphibolite, has the effect of increasing the V_P/V_S ratios, to values of up to 1.78. This can be seen when examining V_P/V_S ratios in samples RK20, RK4 and TW32 (Table 2). In principle, this allows to differentiate between portions of fresh and retrogressed eclogite in subduction channels.

The V_P/V_S values of eclogite appear lower than those of peridotites of the lithospheric mantle of a downgoing slab, quoted for global earth models (1.79; e.g. Kennett et al., 1995), those from experimental studies (e.g. Karato et al., 2008), or those from studies that take compositional differences into account (e.g. Alfonso et al., 2010). High-resolution tomographic analysis of subducting slabs (Northern Honshu; Zhang et al.,2004) shows that the peridotite slab has V_P/V_S ratios of 1.80-1.85 at depths between 60 and 85 km. A zone of lower V_P/V_S ratios (1.70-1.80) in the upper layer of the slab is interpreted to reflect subducted meta-gabbros of the oceanic crust that are transformed to blueschists and/or eclogites. The V_P/V_S values from Zhang et al. (2004) are in good accordance with those derived from the present study, and show that subducted oceanic crust can be imaged and identified by seismic tomography.

The metasediments, however, have much lower V_P/V_S ratios (Table 2), with the exception of the marble sample RK17, which has a V_P/V_S ratio of 1.85. The micaceous rocks and the paragneiss, show V_P/V_S ratios between 1.48 and 1.60, making them typical equivalents of subducted terrigenous sediments deposited in a deep sea trench setting, with V_P/V_S around 1.60 at a V_P velocity of 5 km/s (e.g. Fig. 7 of Tsuji et al., 2011). When large packets of such sediments are subducted, they should be clearly visible as low V_P/V_S features in seismic tomographic images at convergent margins. This signature may be modified by high fluid pressures (e.g. Eberhart-Phillips et al., 2005; Nugraha and Mori, 2006), but based on only the composition of subducted sediments V_P/V_S ratios would be low and coupled with high V_P and V_S anisotropies. For marble, the combination of high V_P/V_S ratio, as well as high V_P anisotropy, and V_P velocities much lower than those of peridotite or eclogite, may constrain a very specific signal for marble, which is a characteristic of subducted carbonate platforms (see e.g. Urai et al., 1990, Behrmann and Seckel, 2007, for a fossil geological example).

6.5 Seismic imaging of subduction channel rocks

The EZ is a good example for a fossilized subduction channel and the data discussed in the previous sections yield important information on the elastic properties of rocks within such a tectonic regime. Nevertheless, no serpentinite is found in this unit, which occurs in several other exhumed subduction channels (e.g. the Voltri Massif in the Western Alps; Frederico et al., 2007, or the Sierra del Convento in Cuba; Blanco-Quintero et al., 2010). Therefore the EZ represents a specific type of subduction channel, in which the viscous matrix surrounding the eclogite boudins is purely made up of high pressure metasediments.

Our results demonstrate that in this kind of subduction channel a matrix of highly anisotropic (up to 7.5 %) metasediments with low V_P (6.2-6.4 km/s) and low V_P/V_S ratios (1.48-1.60) can be expected. At depth of over 45-50 kms, where eclogite high pressure asseblages are stable, the eclogite boudins in

the subduction channel exhibit low anisotropy (~1.5%), high V_P (8.0-8.3 km/s) and a relatively high V_P/V_S ratio (~1.70). At higher levels in the subduction channel, retrogression of the eclogites increases their anisotropy to up to 3.7%, mostly lowers their velocity (7.1-7.6 km/s) and somewhat increases their V_P/V_S ratio (~1.78). This shows that retrogression of eclogite boudins in the subduction channel may be detectable. Marbles in the subduction channel, which originate from subducted carbonate platforms (e.g. e.g. Urai et al., 1990, Behrmann and Seckel, 2007), yield an anisotropy of about 5% and a V_P of about 6.9 km/s. Further, their V_P/V_S ratio is very high with values of 1.85, constraining a specific seismic signal for marble.

The present state of instrumental techniques only permits relatively low resolution images at depths in which high pressure subduction channels are active. Yet, substantial progress was made improving the resolution of seismic imaging in the last decades and it is assumable that a detection of the internal structures within subduction channels will be possible in the future.

In addition, the expected signal of subduction channels can be evaluated by numerical modeling of seismic waves. Essen et al. (2009) modeled subduction channels as a layer of intermediate velocity above the downgoing slab to predict the seismic signal, and showed that high amplitudes of guided waves could indicate the existence of a subduction channel. However, no internal structure within this layer was incorporated in their model. Recent numerical simulations of Friedrich et al. (2014) included a more detailed subduction channel structure with eclogite blocks in a serpentinite matrix. The authors demonstrated that this internal structure leads to very specific seismic signatures. In their model, elastic anisotropy of the rocks was neglected, since the large-scale anisotropy of the subduction channel was considered insignificantly small. Our results show that anisotropy of subduction channel rocks can be significent in case of the metasedimentary matrix surrounding the eclogite blocks. An incorporation of anisotropy in numerical simulations could, therefore, help to make the resulting images more realistic.

7. Conclusion

We use crystallographic preferred orientations (CPO) of a comprehensive suite of rocks from the Tauern Eclogite Zone in southern Austria as a petrophysical analogue for a subduction channel between the downgoing and overriding plates at modern convergent margins. Using this analogy we show in particular that:

1. Time-of-flight neutron diffraction studies on large polymineralic rock samples and the application of full pattern fit methods are a valuable quantitative tool to assess CPO and resulting elastic anisotropy and V_P/V_S ratios of mineralogically complex rocks.
2. P-wave anisotropies of fresh deformed eclogites are fairly low, with an average of about 1.5%, and mainly constrained by pronounced omphacite CPO. Growth and deformation of

retrograde amphibole also produces a pronounced CPO, raising P-wave velocity anisotropy to up to 3.7%, and possibly changing the orientations of velocity maxima.

3. Elastic anisotropies of the once subducted metasediments are higher (up to 7.4%) and constrained by quartz and mica CPO in clastics.
4. Most rock types of such subduction channels have distinct signatures of V_P/V_S ratios. Fresh eclogites can be distinguished from retrogressed ones, and both rock types can in turn be distinguished from mantle peridotites and metasediments of the downgoing lithospheric slab.
5. Subducted terrigenous sediments are not only strongly anisotropic, but also have low V_P/V_S ratios. This makes them detectable at depth in active subduction channels using seismic tomography. Marbles, which may constitute subducted marine carbonates, are distinguishable from terrigenous clastics by high anisotropy, but also high V_P/V_S ratios.

ACKNOWLEDGEMENTS:

Funding by the German Federal Ministry of Education and Research (BMBF) through grants 05K09FKA and 05K13FKB is gratefully acknowledged. We kindly thank Dr. Tatiana Ivankina and the anonymous reviewer for their constructive and helpful comments. We are also grateful to the Frank Laboratory of Neutron Physics (FLNP) at Dubna (Russia) for support in the texture measurements.

FIGURE CAPTIONS:

Figure 1: Tectonic maps of A) the Alps, B) the Tauern Windom (after Schmid et al., 2013) and C) the Eclogite Zone (after Neufeld et al., 2008). The location of the field area is indicated by a frame.

Figure 2: Geologic map of the Eclogite Zone in the area of the Timmeltal (own mapping completed by map of Raith et al., 1980). Sample locations and corresponding dipping angles are indicated in red.

Figure 3: Crystal structures and P-wave velocity distribution of important mineral phases influencing elastic anisotropy of the samples in this study. Colour bars indicate velocity ranges. A = (Vmax-Vmin)/Vmean: anisotropy. Crystallographic axes are indicated.

Figure 4: Typical BSE microstructures of fresh (RK1 and MS112) and retrogressed (RK20, RK49 and RK3) eclogite samples. Czo = clinozoisite; Dol = dolomite; Grt = garnet; Hbl = hornblende; Ky = kyanite; Omp = omphacite; Pg = paragonite; Phe = phengite; Qz = quartz; Rt = rutile. Sections are perpendicular to the foliation and parallel to the stretching lineation. For sample descriptions see table 1.

Figure 5: Micrographs of typical clastic metasediments. Left: micaquartzite (RK6); Right: paragneiss (RK28), both exhibiting a pronounced mica foliation. Sections are perpendicular to the foliation and parallel to the stretching lineation; crossed polarizers.

Figure 6: Recalculated pole figures of omphacite, hornblende, and mica of the retrogressed eclogite samples. Pole figures are oriented according to omphacite lineation and foliation. The lineation (X-direction of the finite strain ellipsoid) is EW in the pole figure, the foliation normal (Z-direction of the finite strain ellipsoid) is oriented NS, and the Y-direction (perpendicular to X and Z) lies normal to the pole figure plane. Pole figures are lower hemisphere equal area projections. Contour levels are multiples of a random distribution. Only significant pole figures are given. They are sufficient to illustrate he textural differences between samples.

Figure 7: Recalculated pole figures of omphacite, garnet, mica, and quartz of fresh eclogite samples. Pole figures are oriented according to omphacite lineation and foliation. The lineation (x-direction) is EW in the pole figure, foliation normal (z-direction) is oriented NS and the y-direction (perpendicular to x and z) lies normal to the pole figure plane. All pole figures are lower hemisphere equal area projections. Contour levels are multiples of a random distribution.

Figure 8: Recalculated pole figures of quartz, mica and calcite in the metasedimetary samples. The pole figures of the clastic metasedimentary samples (RK5, RK6, and RK28) are oriented according to the mica lineation and foliation, whereas the marble sample (RK17) is aligned with respect to the calcite lineation and foliation. The lineation (x-direction) is EW in the pole figure, foliation normal (z-direction) is oriented NS and the y-direction (perpendicular to x and z) lies normal to the pole figure plane. Pole figures are lower hemisphere equal area projections. Contour levels are multiples of random distribution.

Figure 9: (A) Calculated and experimental P-wave velocity distributions. The experimental data was gained at confining pressures of 300 MPa (TW32) and 400 MPa (TW33). HP: velocity distributions calculated for the corresponding high pressure assemblage of retrogressed samples RK4 and RK20. Cold colours indicate high velocities, warm colours low velocities, black lines indicate distinct contour levels and contour level spacings. (B) Minimum (circles) and maximum (squares) experimantal P-wave velocity at increasing pressures. Grey bar indicates calculated P-wave velocity.

Figure 10: Equilibrium assemblage diagram (pseudosection) of sample RK20, illustrating the modelled high-pressure parageneses. Whole rock chemistry is given in upper right corner. Parageneses containig glaucophane are blue-coloured, the enhanced subvertical line defines the onset of lawsonite stability towards cooler temperatures. The eclogite facies mineral assemblage Grt+Omph+Phng+Qtz+Ru occupies a large stability field and shows only minor changes in modal mineral amounts. Thin solid and short dashed lines are contours of volume percentage of omphacite and garnet, respectively. The long dashed line represents the transformation of quartz to coesite. The bright rectangle in the center outlines estimated peak metamorphic conditions of the EZ (Stöckert et al., 1997; Hoschek, 2001; 2004), the arrow indicates the retrograde metamorphic path of the EZ (Kurz et al., 1998).

Sample	Description	Composition
RK1	Layered, mica-rich eclogite with medium grain size. Alternating omphacite, garnet, and mica layers of 0.5-4 mm.	37 % omphacite, 19 % zoisite, 15 % garnet, 15 % phengite, 7 % quartz, 4 % dolomite, 3 % rutile
RK3	Fine-grained eclogite with weak layering.	43 % omphacite, 22 % garnet, 15 % paragonite, 10 % glaucophane, 9 % quartz, 1 % rutile
RK4	Retrogressed eclogite with pronounced carbonate-rich layers. Medium grain size and layers of about 1-5 mm	37 % barroisite, 25 % omphacite, 12 % phengite, 9 % garnet, 8 % albite, 6 % dolomite, 3 % calcite
RK4HP	Simulated HP equivalent of sample RK4	38 % omphacite, 33 % garnet, 12 % phengite, 8 % quartz, 6 % magnesite (MgCO3), 3 % dolomite
RK5	Layered micaschist, containing clinozoisite.	71 % quartz, 24 % muscovite, 5 % clinozoisite
RK6	Micaquartzite	92 % quartz, 8 % muscovite
RK17	Medium-grained, foliated marble	99 % calcite, 1 % dolomite
RK20	Coarse-grained eclogite with omphacite-dominated and garnet-dominated layers of 5-10 mm.	43 % omphacite, 24 % garnet, 20 % glaucophane, 7 % quartz, 3 % albite, 2 % paragonite, 1 % rutile
RK20HP	Simulated HP equivalent of sample RK4	52 % omphacite, 23 % garnet, 13 % phengite, 11 % quartz, 1 % rutile
RK28	Paragneiss with strong mica foliation.	50% quartz, 31 % albite, 19 % muscovite
RK49	medium-grained, layered, retrogressed eclogite.	25 % omphacite, 33 % albite, 14 % garnet, 12 % phengite, 8 % quartz, 8 % glaucophane
MS11.2	Fine-grained, mylonitized eclogite with pronounced layering of omphacite and garnet. Layers are 0.5-2 mm thick.	45 % omphacite, 24 % almandine, 15 % quartz, 6 % phengite, 5 % albite, 4 % glaucophane, 1 % rutile
TW32	Weakly layered, medium grained amphibolite.	51 % hornblende, 20% paragonite, 8 % garnet, 6 % albite, 5 % dolomite, 5 % chlorite, 3 % omphacite, 2 % quartz
TW33	Layered, mica-rich eclogite with fine to medium grain size.	38 % omphacite, 24 % garnet, 19 % phengite, 10 % albite, 5 % glaucophane, 4 % quartz

Table 1: Description and modal compositions of the investigated samples, derived from RTA. RK4HP and RK20HP are model compositions calculated by means of the THERIAK/DOMINO thermodynamic modeling tool.

	Sample	Lithology	**Vp_{iso} (km/s)**	min	max	Ap (%)	**Vs_{iso} (km/s)**	Vs1 min	Vs1 max	Vs2 min	Vs2 max	**Vp/Vs**
A	RK1	Eclogite	8.03	8.01	8.05	0.4	4.68	4.68	4.69	4.67	4.68	1.71
	RK3	Eclogite	8.14	8.08	8.22	1.8	4.77	4.76	4.80	4.75	4.78	1.71
	RK4	Strongly retro-gressed Eclogite	7.54	7.48	7.56	1.2	4.25	4.26	4.26	4.252	4.26	1.77
	RK4HP	Eclogite	8.27	8.23	8.29	0.7	4.81	4.81	4.82	4.80	4.81	1.72
	RK5	Micaschist	6.39	6.16	6.64	7.4	4.18	4.11	4.40	4.03	4.21	1.53
	RK6	Micaquartzite	6.24	6.07	6.39	5.3	4.22	4.20	4.38	4.05	4.28	1.48
	RK17	Marble	6.86	6.62	6.97	5.1	3.72	3.64	3.75	3.62	3.67	1.84
	RK20	Retrogressed Eclogite	7.57	7.49	7.77	3.7	4.38	4.36	4.43	4.35	4.39	1.73
	RK20HP	Eclogite	7.40	7.31	7.48	2.3	4.23	4.23	4.26	4.22	4.24	1.75
	RK28	Paragneiss	6.37	6.12	6.54	6.8	3.98	3.93	4.10	3.88	3.97	1.60
	RK49	Eclogite	7.46	7.41	7.52	1.4	4.30	4.26	4.33	4.26	4.31	1.74
	MS11.2	Eclogite	8.12	8.05	8.16	1.5	4.78	4.73	4.78	4.72	4.76	1.70
	TW32	Amphibolite	7.14	7.05	7.23	2.6	4.01	4.00	4.05	3.98	4.02	1.78
	TW33	Eclogite	8.00	7.88	8.11	2.9	4.62	4.58	4.68	4.57	4.63	1.73
B	TW32	Amphibolite	7.25	7.01	7.43	4.4						
	TW33	Eclogite	7.56	7.28	7.91	8.3						

Table 2: P-wave (Vp) and S-wave (Vs) velocities, elastic anisotropies (A) and Vp/Vs ratio of all samples. A: Modelled from CPO of the samples. B: experimentally measured. Mean values for Vp and Vs were calculated by averaging the three measured or modeled principal velocites.

REFERENCES:

Ábalos, B., Fountain, D.M., Gil Ibarguchi, J.I., Puelles, P., 2010. Eclogite as a seismic marker in subduction channels: Seismic velocities, anisotropy, and petrofabric of Cabo Ortegal eclogite tectonites (Spain). GSA Bulletin,123, 3/4, 439–456.

Agard, P., Yamato, P., Jolivet L., and Burov, E., 2009. Exhumation of oceanic blueschists and eclogites in subduction zones: Timing and mechanisms, Earth Science Review, 92, 53–79.

Aleksandrov, K.S., Ryzhova, T.V., 1961. The elastic properties of rock forming minerals. Izvestija Academy of Science USSR, Geophysical Ser. 12, 1799–1804.

Aleksandrov, K.S., Alchikov, U.V., Belikov, B.P., Zaslavski, B.I., and Krupny, A.I., 1974. Elastic wave velocities in minerals at atmospheric pressure and increasing precision of elastic constants by means of EVM. Izvestija Academy of Science USSR, Geological Series, 10, 15-24.

Anczkiewicz, R., Platt, J. P., Thirlwall, M. F., Wakabayashi, J., 2004. Franciscan subduction off to a slow start: evidence from high-precision Lu–Hf garnet ages on high grade-blocks. Earth and Planetary Science Letters, 225, 147– 161.

Angiboust, S., Agard, P., Jolivet, L., Beyssac, O., 2009. The Zermatt–Saas ophiolite: the largest (60-km wide) and deepest (c. 70–80 km) continuous slice of oceanic lithosphere detached from a subduction zone? Terra Nova 21, 171–180.

Babuska, V., Fiala, J., Kumazawa, M., Ohno, I., and Sumino, Y., 1978. Elastic properties of garnet solid-solution series. Physics of the Earth and Planetary Interiors, 16, 157–176.

Barruol, G. and Kern H., 1996. Seismic anisotropy and shear-wave splitting in lower-crustal and upper-mantle rocks from the Ivrea Zone experimental and calculated data. Physics of the Earth and Planetary Interiors, 95, 175-194.

Bascou, J., Barruol, G., Vauchez, A., Mainprice, D., Egydio-Silva, M., 2001. EBSD-measured lattice preferred orientations and seismic properties of eclogites. Tectonophysics, 342, 61–80.

Behrmann, J.H., 1984. Microstructure and chemistry of white mica in a low grade mylonite. Journal of Structural Geology, 6, 283-292.

Behrmann, J.H., Ratschbacher, L., 1989. Archimedes revisited: a structural test of eclogite emplacement models in the Austrian Alps. Terra Nova 1, 242–252.

Behrmann, J.H., Seckel, C., 2007. Structural analysis of the Small Cyclades Iraklia and Schinoussa (Aegean Sea, Greece). Geotectonic Research, 95, 1-11.

Bezacier L., Reynard B., Bass J.D., Wang J., Mainprice D., 2010. Elasticity of glaucophane, seismic velocities and anisotropy of the subducted oceanic crust. Tectonophysics 494, 201-210.

Bhagat, S.S., Bass, J.D., and Smyth, J.R., 1992. Single-crystal elastic properties of omphacite-C2/C by Brillouin spectroscopy. Journal of Geophysical Research–Solid Earth, 97, 6843–6848.

Blanco-Quintero, I.F., García-Casco, A. and Gerya, T.V., 2010. Tectonic blocks in serpentinite mélange (eastern Cuba) reveal large-scale convective flow of the subduction channel. Geology, 39, 79-82.

Bousquet, R., 2008. Metamorphic heterogeneities within a single HP unit: Overprint effect or metamorphic mix? Lithos, 103, 46-69.

Brown, J.M., Abramson, E.H., and Angel, R.J., 2006. Triclinic elastic constants for low albite. Physics and Chemistry of Minerals, 33, 256-265.

Brown, D., Llana-Fúnez, S., Carbonell, R., Alvarez-Marron, J., Marti, D., and Salisbury, M.H., 2009. Laboratory measurements of P-wave and S-wave velocities across a surface analog of the continental crust-mantle boundary: Cabo Ortegal, Spain. Earth and Planetary Science Letters, 285, 27–38.

Christoffel, E.B., 1874. Über die Fortpflanzung von Stössen durch elastische, feste Körper. Annali de Matematica, 8, 193-243.

Christensen, N.I., 1974. Compressional wave velocities in possible mantle rocks to pressures of 30 kbars. Journal of Geophysical Research 79, 407–412.

Cloos, M. and Shreve, R. L., 1988. Subduction-Channel Model of Prism Accretion, Melange Formation, Sediment Subduetion, and Subduction Erosion at Convergent Plate Margins: Implications and Discussion, Pure and Applied Geophysics 128, 314, 501-545.

Dachs, E., 1990. Geothermobarometry in metasediments of the southern Grossvenediger area (Tauern Window, Austria). Journal of Metamorphic Geology, 8, 217–230.

Dandekar, D.P., 1968. Variation in the elastic constants of calcite with pressure. American Geophysical Union Transactions, 49, 323 pp.

De Capitani, C., and Brown, T.H., 1987. The computation of chemical equilibrium in complex systems containing non-ideal solutions. Geochimica et Cosmochimica Acta, 51, 2639-2652.

De Capitani, C., and Petrakakis, K., 2010. The computation of equilibrium assemblage diagrams with Theriak/Domino software. American Mineralogist, 95, 1006-1016.

De Franco, R., Govers, R., Wortel, R., 2008. Nature of the plate contact and subduction zones diversity. Earth and Planetary Science Letters, 271, 245–253.

Eberhart-Phillips, D., Reyners, M., Chadwick, M., Chiu, J.-M., 2005. Crustal heterogeneity and subduction processes: 3-D *Vp, Vp/Vs* and *Q* in the southern North Island, New Zealand. Geophysical Journal International, 162, 270-288.

Essen, K., Braatz, M., Ceranna, L., Friederich, W. and Meier, T., 2009. Numerical modelling of seismic wave propagation along the plate contact of the Hellenic Subduction Zone—the influence of a deep subduction channel. Geophysical Journal International, 179, 1737–1756.

Fountain, D.M., Boundy, T.M., Austrheim, H., and Rey, P., 1994. Eclogite–facies shear zones—deep crustal reflectors? Tectonophysics, 232, 411– 424.

Frederico, L., Crispini, L., Scambelluri, M. and Capponi, G., 2007. Ophiolite mélange zone records exhumation in a fossil subduction channel. Geology, 35, 499-502.

Friederich, W., Lambrecht, L., Stöckhert, B., Wassmann, S. and Moos, C., 2014. Seismic visibility of a deep subduction channel – insights from numerical simulation of high-frequency seismic waves emitted from intermediate depth earthquakes. Solid Earth, 5, 141–159.

Gao, S., Kern, H., Jin, Z., Popp, T., Jin, S., Zhang, H., Zhang, B., 2001. Poisson's ratio of eclogite: the role of retrogression. Earth and planetary Science Letters, 102, 523–531.

Glodny, J., Ring, U., Kühn, A., Gleissner; P., Franz, G., 2005. Crystallization and very rapid exhumation of the youngest Alpine eclogites (Tauern Window, Eastern Alps) from Rb/Sr mineral assemblage analysis. Contributions to Mineralogy and Petrology, 149, 699 – 712.

Guillot, S., Hattori, K., Sigoyer, J., Nägler, T., Auzende, A.L., 2001. Evidence of hydration of the mantle wedge and ist role in the exhumation of eclogites. Earth Planet Scientific Letters 193: 115–127.

Helmstaedt, H., Anderson, D.L., and Gavasci, A.T., 1972. Petrofabric studies of eclogite, spinel websterite, and spinel-lherzolite xenoliths from kimberlite-bearing breccia pipes in southeastern Utah and northeastern Arizona. Journal of Geophysical Research, 77, 4350–4365.

Heyliger, P., Ledbetter, H., Kim, S., 2003. Elastic constants of natural quartz. Journal of the Acoustical Society of America, 114, 644-650.

Hill, R., 1952. The elastic behavior of a crystalline aggregate. Proceedings of the Physical Society, A65, 349-354.

Holland, T.J.B., Powell, R., 1998. An internally-consistent thermodynamic dataset for phases of petrological interest. Journal of Metamorphic Geology, 16, 309-344.

Hoschek, G., 2001. Thermobarometry of metasediments and metabasites from the Eclogite zone of the Hohe Tauern, Eastern Alps, Austria. Lithos, 59, 127-150.

Hoschek, G., 2004. Comparison of calculated P-T pseudosections for a kyanite eclogite from the Tauern Window, Eastern Alps, Austria. European Journal of Mineralogy 16, 59-72.

Ivankina T.I., Kern H.M., Nikitin A.N., 2005. Directional dependence of P- and S-wave propagation and polarization in foliated rocks from the Kola superdeep well: Evidence from laboratory measurements and calculations based on TOF neutron diffraction. Tectonophysics, 407, 25-42.

Karato, S., Jung, H., Katayama, I., Skemer, P., 2008. Geodynamic significance of seismic anisotropy of the upper mantle: new insights from laboratory studies. Annual Review of Earth and Planetary Sciences, 36, 59–95.

Kennett, B.L.N., Engdahl, E.R., Buland R, 1995. Constraints on seismic velocities in the Earth from travel times. Geophys. J. Int., 122, 108-124.

Keppler, R., Ullemeyer, K., Behrmann, J.H. & Stipp, M., 2014. Potential of full pattern fit methods for the texture analysis of geological materials: implications from texture measurements at the recently upgraded neutron time-of-flight diffractometer SKAT. Journal of Applied Crystallography, 47, doi:10.1107/S1600576714015830.

Kern, H., Gao, S., Jin, Z., Popp, T., Jin, S., 1999. Petrophysical studies on rocks from the Dabie ultrahigh-pressure (UHP) metamorphic belt, Central China: implications for the composition and delamination of the lower crust. Tectonophysics, 301, 191–215.

Kern, H., Jin, Z., Gao, S., Popp, T., and Xu, Z., 2002. Physical properties of ultrahigh-pressure metamorphic rocks from the Sulu terrain, eastern central China: Implications for the seismic structure at the Donghai (CCSD) drilling site. Tectonophysics, 354, 315– 330.

Kern, H., Ivankina, T.I., Nikitin, A.N., Lokajíček, T., Pros, Z., 2008. The effect of oriented microcracks and crystallographic and shape preferred orientation on bulk elastic anisotropy of a foliated biotite gneiss from Outokumpu. Tectonophysics, 457, 143–149.

Kitamura, K., 2006. Constraint of lattice-preferred orientation (LPO) on Vp anisotropy of amphibole-rich rocks. Geophysical Journal International, 165, 1058–1065.

Kurz, W., and Froitzheim, N., 2002. The exhumation of eclogite-facies metamorphic rocks - A review of models confronted with examples from the Alps. International Geological Review, 44, 8, 702-743.

Kurz, W., Neubauer, F., Genser, J., Dachs, E. 1998. Alpine geodynamic evolution of passive and active continental margin sequences in the Tauern Window (eastern Alps, Austria, Italy): a review. International Journal of Earth Sciences, 87, 225–242.

Llana-Fúnez, S., and Brown, D., 2012. Contribution of crystallographic preferred orientation to seismic anisotropy across a surface analog of the continental Moho at Cabo Ortegal, Spain. GSA Bulletin, 124, 9/10, 1495–1513.

Lutterotti, L., Matthies, S., Wenk, H.-R., Schultz, A. J., and Richardson, J. W., 1997. Combined texture and structure analysis of deformed limestone from time-of-flight neutron diffraction spectra. Journal of Applied Physics 81, 594–600.

Mainprice, D., and Humbert, M., 1994. Methods of calculating petrophysical properties from lattice preferred orientation data. Surveys in Geophysics, 15, 575–592.

Mainprice, D., and Ildefonse, B., 2009. Seismic Anisotropy of Subduction Zone Minerals–Contribution of Hydrous Phases. In: S. Lallemand and F. Funiciello (eds.), Subduction Zone Geodynamics, Springer-Verlag Berlin Heidelberg, 63-84.

Matthies, S., 2011. GEO-MIX-SELF calculation of the elastic properties of a textured graphite sample at different hydrostatic pressures. Journal of Applied Crystallography, 45, 1-16.

Matthies, S., and Humbert, M., 1995. On the principle of a geometric mean of even-rank symmetric tensors for textured polycrystals. Journal of Applied Crystallography, 28, 254-266.

Mauler, A., Burlini, L., Kunze, K., Philippot, P., Burg, J.-P., 2000. P-wave anisotropy in eclogites and relationship to the omphacite crystallographic fabric: Physics and Chemistry of the Earth, 15, 119–126.

Meltzer, A., and Christensen, N., 2001. Nanga Parbat crustal anisotropy: Implications for interpretation of crustal velocity structure and shear-wave splitting. Geophysical Research Letters, 28, 10, 2129-2132.

Montagner, J.-P., Guillot, L., 2003. Seismic Anisotropy and global geodynamics. Mineralogical Society of America, 51, 353-385.

Montagner, J.-P., Tanimoto, T., 1990. Global Anisotropy in the Upper Mantle Inferred From the Regionalization of Phase Velocities. Journal of Geophysical Research, 95, B4, 4797-4819.

Nagel, T. J., Herwartz, D., Rexroth, S., Münker, C., Froitzheim, N., Kurz, W., 2013. Lu-Hf dating, petrography, and tectonic implications of the youngest Alpine eclogites (Tauern Windo, Austria). Lithos 170-171, 179-190.

Neufeld, K., Ring, U., Heidelbach, F., Dietrich, S., and Neuser, R.D., 2008. Omphacite textures in eclogites of the Tauern Window: Implications for the exhumation of the Eclogite Zone, Eastern Alps. Journal of Structural Geology, 30, 976–992.

Nugraha, A.D. and Mori, J., 2006. Three-dimensional velocity structure in the Bungo Channel and Shikoku area, Japan, and its relationship to low-frequency earthquakes. Geophysical research letters, 33, doi:10.1029/2006GL028479.

Platt, J.P., 1986. Dynamics of orogenic wedges and the uplift of high pressure metamorphic rocks. Bulletin of the geological Society of America, 97, 1037-1053.

Pros, Z., Lokajícek, T., and Klíma, K., 1998. Laboratory study of elastic anisotropy on rock samples. Pure Applied Geophysics, 151, 619– 629.

Pros, Z., Lokajícek, T., Prikryl, R., Klíma, K., 2003. Direct measurement of 3D elastic anisotropy on rocks from the Ivrea Zone (Southern Alps, NW Italy). Tectonophysics 370, 31– 47.

Punturo, R., Kern, H., Cirrincione, R., Mazzoleni, P., and Pezzino, A., 2005. P- and S-wave velocities and densities in silicate and calcite rocks from the Peloritani ountains, Sicily (Italy): The effect of pressure, temperature and the direction of wave propagation. Tectonophysics, 409, 55-72.

Raith, M., Mehrens, C., and Thöle W., 1980. Gliederung, tektonischer Bau und metamorphe Entwicklung der penninischen Serien im südlichen Venediger-Gebiet, Osttiroler Jahrbuch der Geologischen Bundesanstalt, 123, 1–37.

Ratschbacher, L., Dingeldey, C., Miller, C., Hacker, B. R., McWilliams, M. O., 2004. Formation, subduction, and exhumation of Penninic oceanic crust in the Eastern Alps: time constraints from 40Ar/39Ar geochronology. Tectonophysics, 394, 155– 170.

Reuss, A., 1929. Berechnung der Fließgrenze von Mischkristallen auf Grund der Plastizitätsbedingung für Einkristalle. Zeitschrift für Angewandte Mathematik und Mechanik, 9, 49-58.

Schmädicke, E., Will, T. M., 2003. Pressure–temperature evolution of blueschist facies rocks from Sifnos, Greece, and implications for the exhumation of high-pressure rocks in the Central Aegean. Journal of metamorphic Geologie, 21, 799–811.

Schmid, S. M., Pfiffner, O. A., Froitzheim, N., Schönborn, G., and Kissling, E., 1996. Geophysical-geological transect and tectonic evolution of the Swiss-Italian Alps. Tectonics, 15, 1036–1064.

Schmid, S.M., Scharf, A., Handy, M.R., and Rosenberg, C.L., 2013. The Tauern Window (Eastern Alps, Austria): a new tectonic map, with cross-sections and a tectonometamorphic synthesis. Swiss Journal of Geoscience, 106, 1-32.

Schmid, S.M., Casey, M., 1986. Complete fabric analysis of some commonly observed quartz c-axis patterns. Geophysical Monograph, 36, 263-286.

Shreve, R.L., Cloos, M., 1986. Dynamics of sediment subduction, melange formation, and prism accretion. Journal of Geophysical Research 91 (B10), 10229–10245.

Silver, P.G., 1996. Seismic anisotropy beneath the continents: probing the depths of geology. Annual Review: Earth and Space Science 24, 385.

Stipp, M., Stünitz, H., Heilbronner, R., Schid, S.M., 2002. The eastern Tonale fault zone: a natural laboratory for crystal plastic deformation of quartz over a temperature range from 250 to 700 °C. Journal of Structural Geology, 24, 1861-1884.

Stöckhert, B., Massonne, H.-J., Nowlan, E. U., 1997. Low differential stress during high-pressure metamorphism: the microstructural record of a metapelite from the Eclogite Zone, Tauern Window, Eastern Alps. Lithos, 41, 103-118.

Tsuji, T., Dvorkin, J., Mavko, G., Nakata, N., Matsuoka, T., Nakanishi,A., Kodaira, S., Nishizawa, O., 2011. V_P/V_S ratio and shear-wave splitting in the Nankai Trough seismogenic zone: Insights into

effective stress, pore pressure, and sediment consolidation. Geophysics, 76, WA71–WA82, doi: 10.1190/1.3560018

Ullemeyer K., Siegesmund S., Rasolofosaon P.N.J., Behrmann J.H., 2006. Experimental and texture-derived P-wave anisotropy of principal rocks from the TRANSALP traverse: An aid for the interpretation of seismic field data. Tectonophysics, 414, 97-116.

Ullemeyer, K., Spalthoff, P., Heinitz, J., Isakov, N. N., Nikitin, A. N., Weber, K., 1998. The SKAT texture diffractometer at the pulsed reactor IBR-2 at Dubna: Experimental layout and first measurements. Nuclear Instruments and Methods of Physical Research, 412, 80–88.

Ullemeyer, K, Leiss, B. and Stipp, M., 2010. Textures and Microstructures in Peridotites from the Finero Complex (Ivrea Zone, Alps) and their Influence on the Elastic Rock Properties. Solid State Phenomena, 160, 183-188.

Ullemeyer, K., Nikolayev, D.I., Christensen, N.I., and Behrmann, J.H., 2011. Evaluation of intrinsic velocity-pressure trends from low-pressure P-wave velocity measurements in rocks containing microcracks. Geophysical Journal International 185, 1312–1320.

Urai, J.L., Schuiling, R.D., Jansen, J.B.H., 1990. Alpine Deformation on Naxos (Greece). In: Knipe, R.J., Rutter, E.H. (Eds.): Deformation mechanisms, rheology and tectonics. Spec. Publ. Geol. Soc. London 54: 509–522.

Vaughan, M.T, Guggenheim, S., 1986. Elasticity of muscovite and its relationship to crystal structure. Journal of Geophysical Research 91, 4657– 4664.

Voigt, W., 1928. Lehrbuch der Kristallphysik, Teubner, Leipzig.

Wenk, H.-R., Lutterotti, L. and Vogel, S. C., 2010. Rietveld texture analysis from TOF neutron diffraction data. Powder Diffraction 25, 3, 283-296.

Wenk, H. R., Takeshita, T., Bechler, E., Erskine, B.G. and Matthies, S., 1987. Pure shear and simple shear calcite textures. Comparison of experimental, theoretical and natural data. Journal of Structural Geology, 9, 731–745.

Wenk, H.-R., Vasin, R.N., Kern, H., Matthies, S., Vogel, S.C., Ivankina, T.I., 2012. Revisiting elastic anisotropy of biotite gneiss from the Outokumpu scientific drill hole based on new texture measurements and texture-based velocity calculations. Tectonophysics, 570–571, 123–134.

Worthington, J.R., Hacker, B.R., Zandt, G., 2013. Distinguishing eclogite from peridotite: EBSD-based calculations of seismic velocitites. Goephysical Journal International – Seismology. doi: 10.1093/gji/ggt004

Zappone, A., Fernàndez, M., García-Duenas, V., and Burlini, L., 2000. Laboratory measurements of seismic P-wave velocities on rocks from the Betic chain (southern Iberian Peninsula). Tectonophysics, 317, 259-272.

Zhang, X. L., Hu, L., Ji, M., Liu, J.L. and Song, H.L., 2013. Microstructures and deformation mechanisms of hornblende in Guandi complex, the Western Hills, Beijing. Science China, Earth Sciences, 56, 9, 1510-1518.

Zhang, H., Thurber, C.H., Shelly, D., Ide, S., Beroza, G.C., Hasegawa, A., 2004. High-resolution subducting-slab structure beneath northern Honshu, Japan, revealed by double-difference tomography. Geology, 42, 361-364. doi: 10.1130/G20261.2

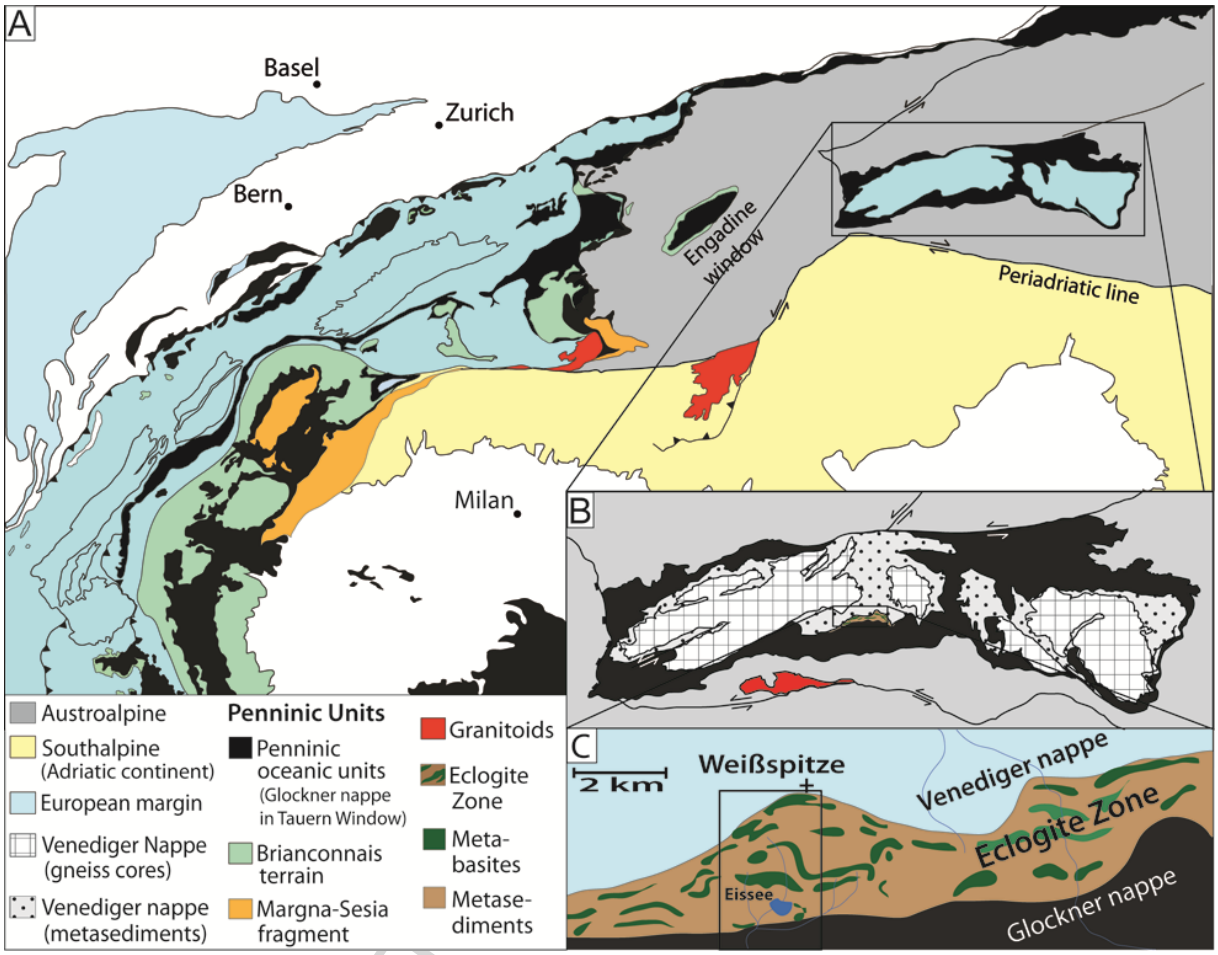

Figure 1

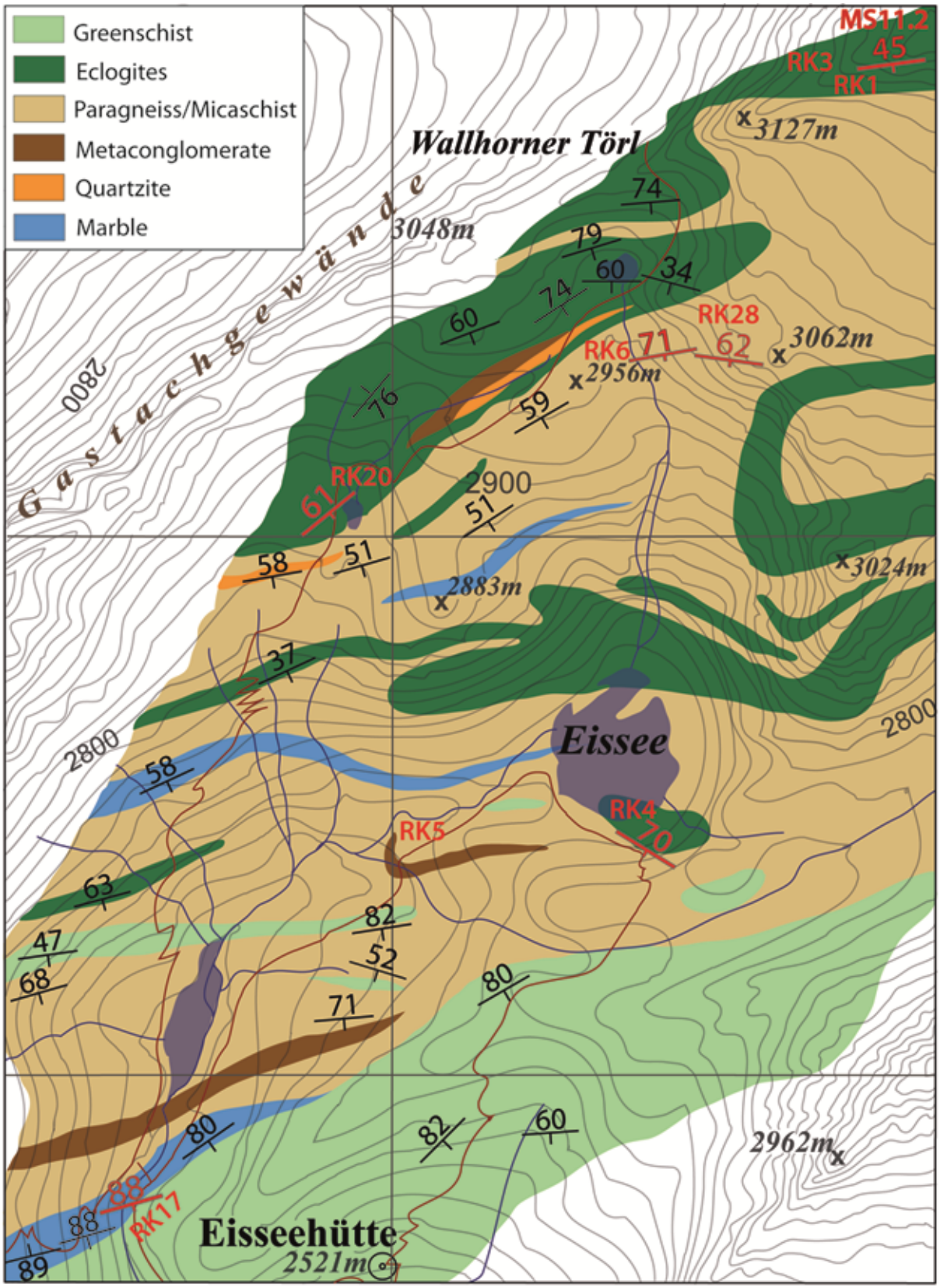

Figure 2

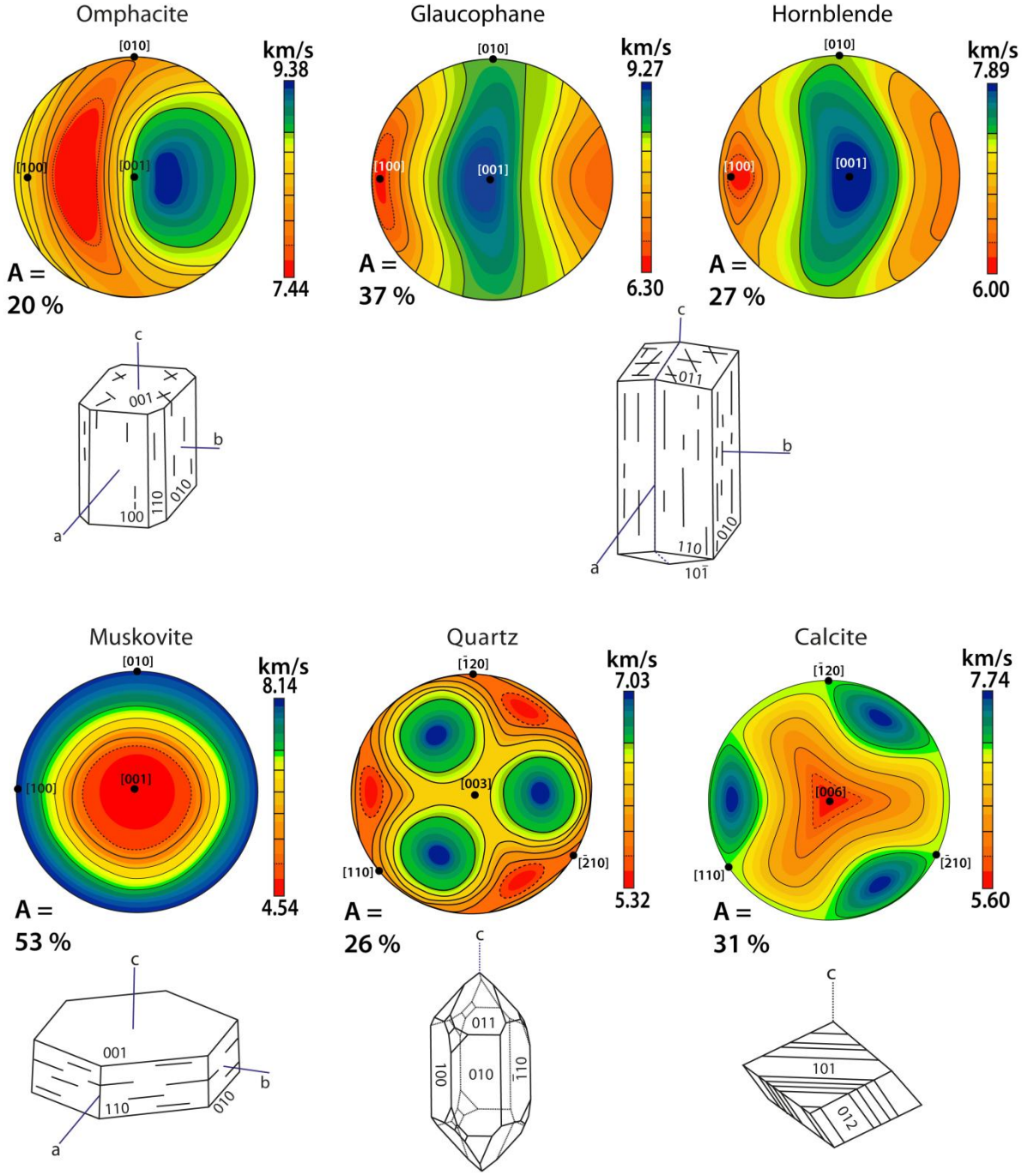

Figure 3

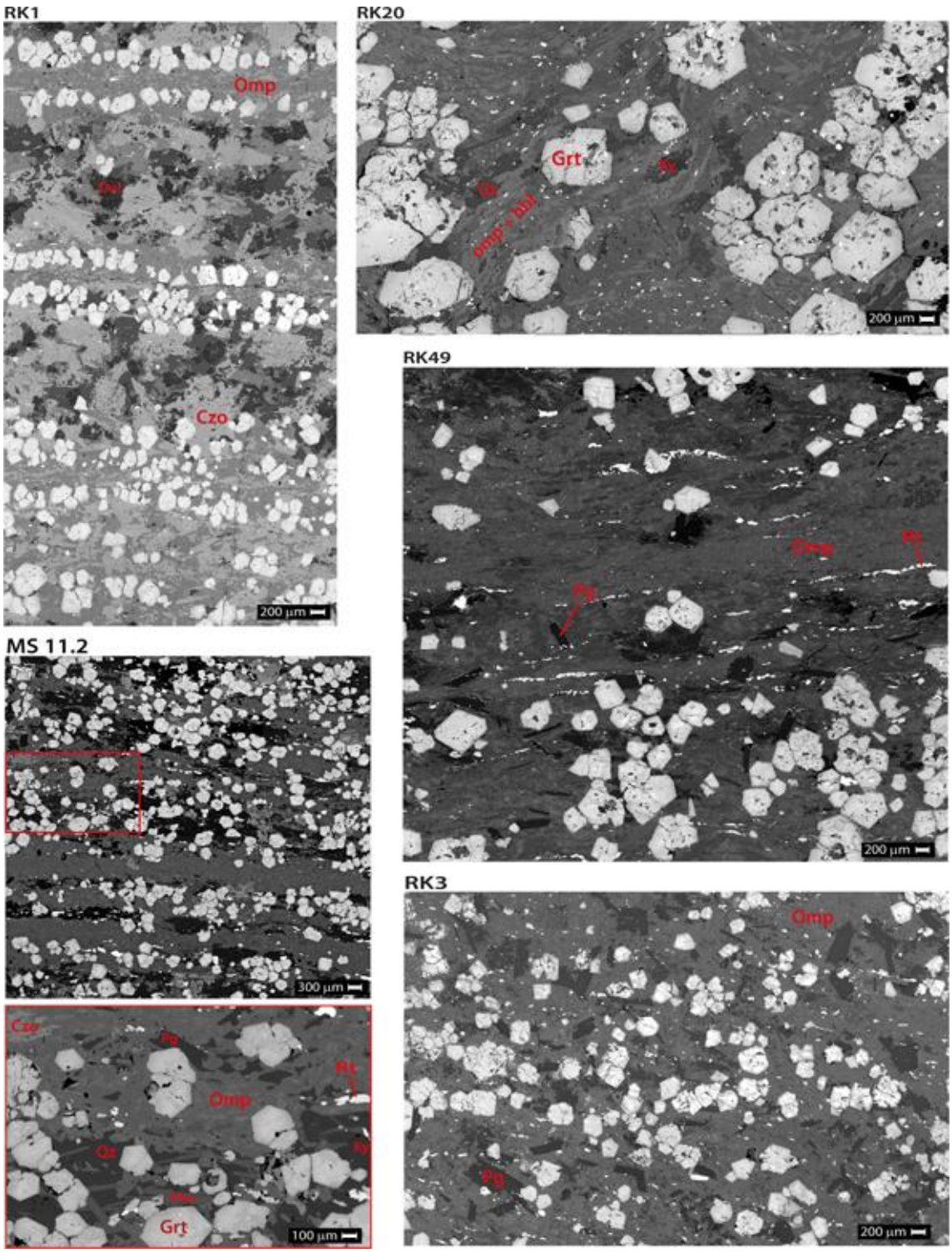

Figure 4

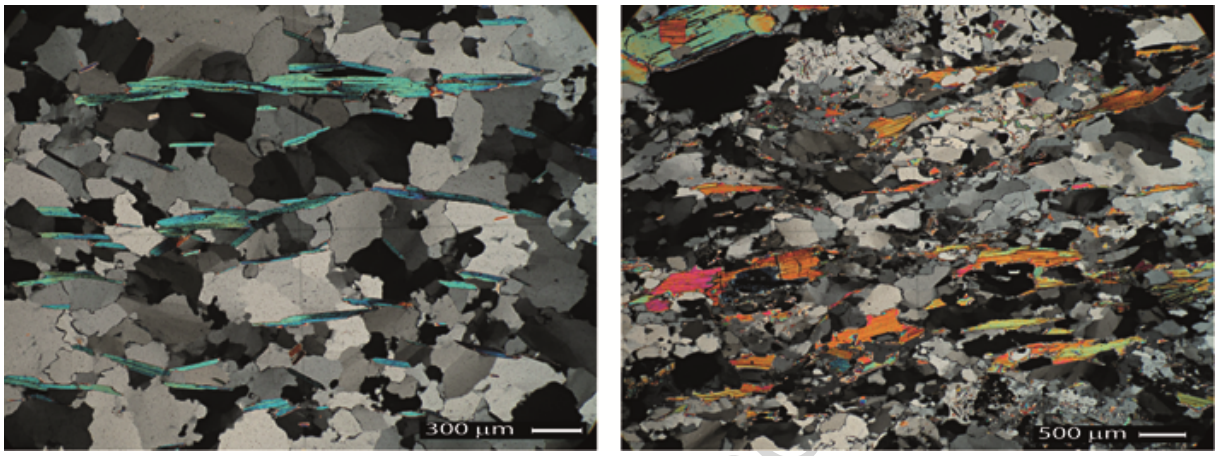

Figure 5

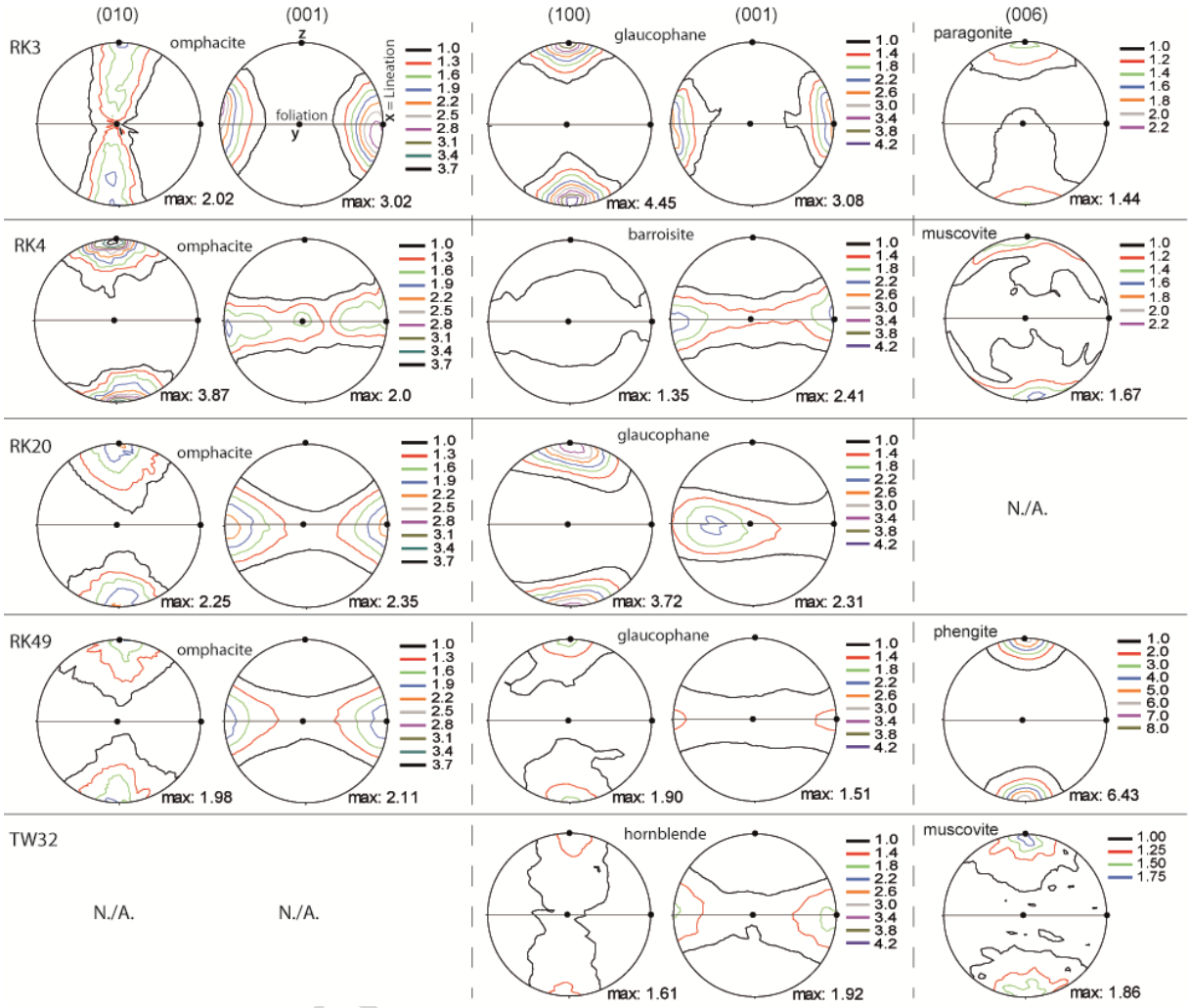

Figure 6

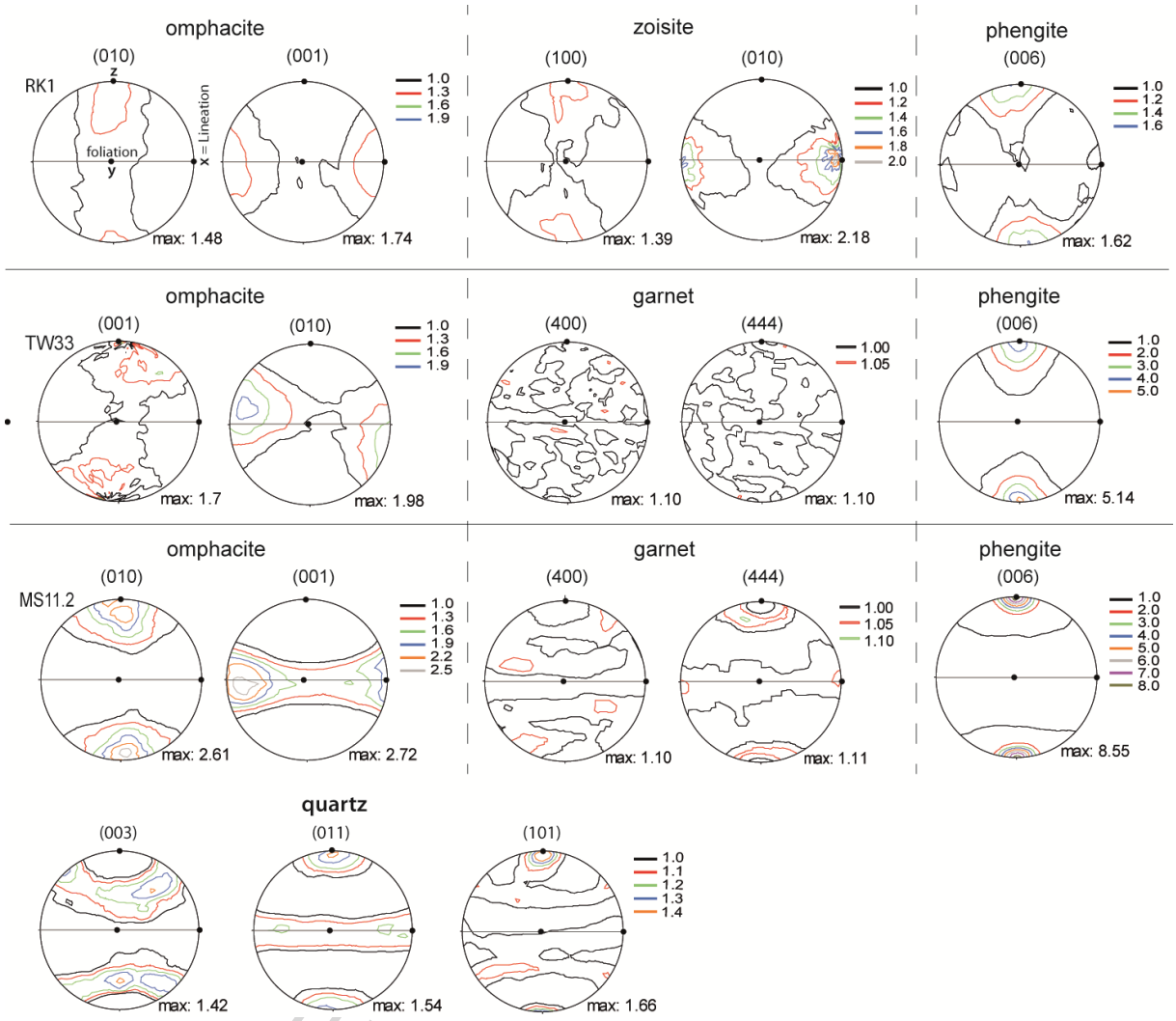

Figure 7

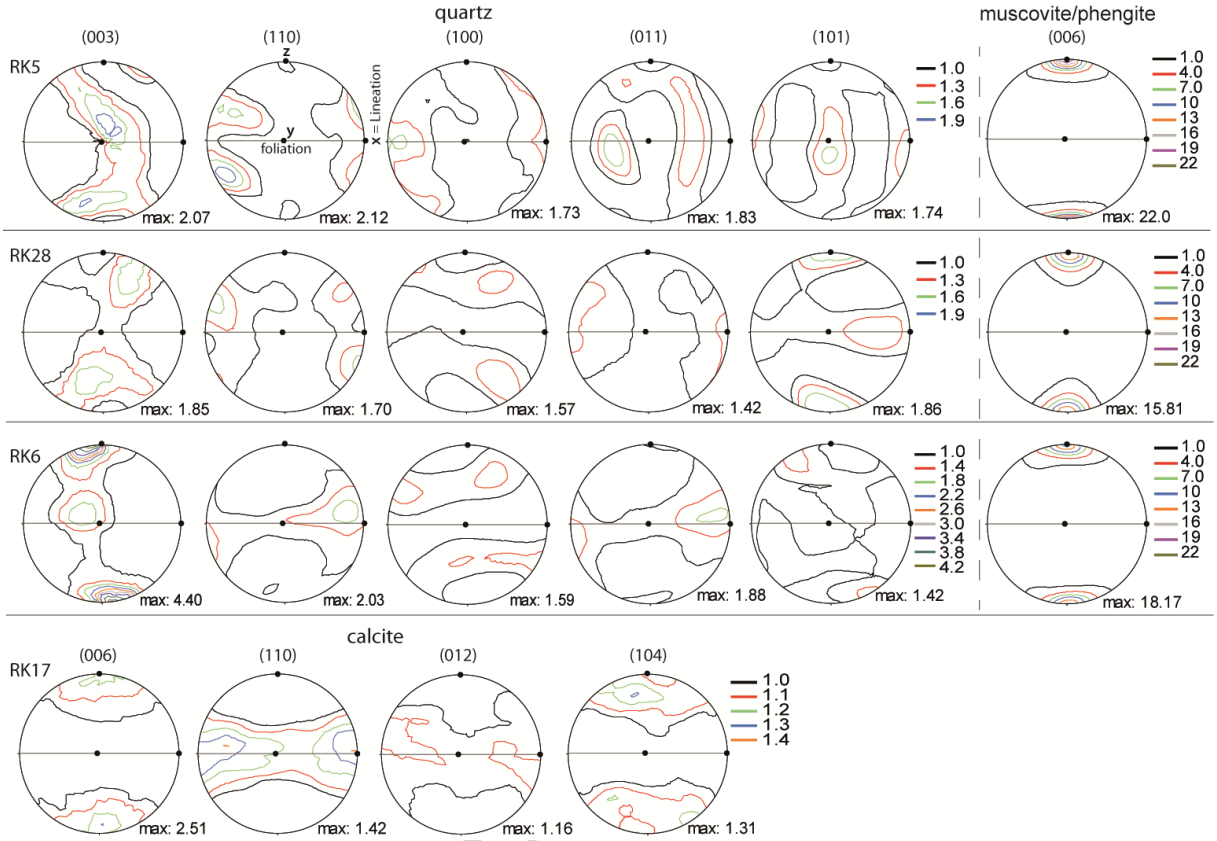

Figure 8

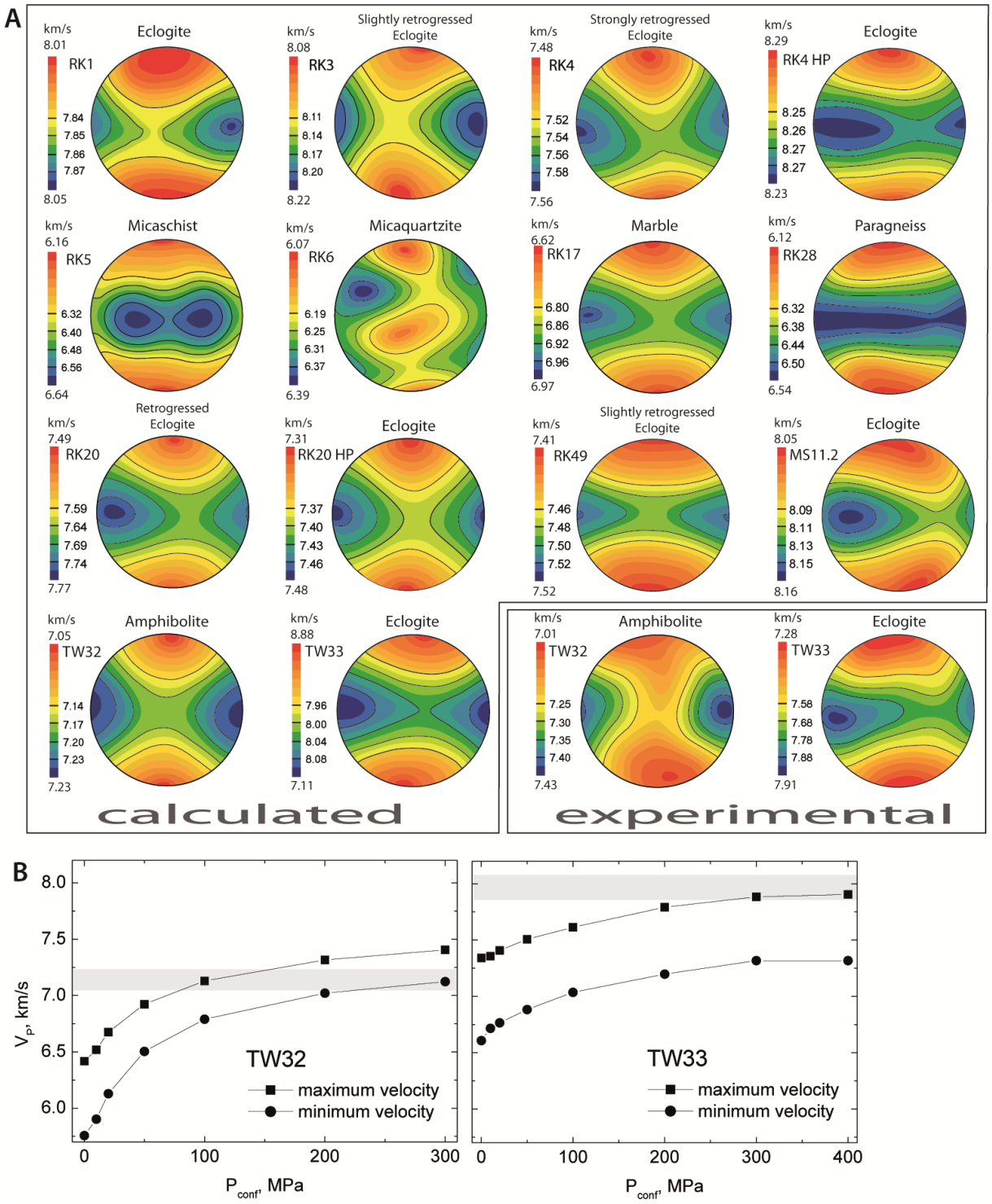

Figure 9

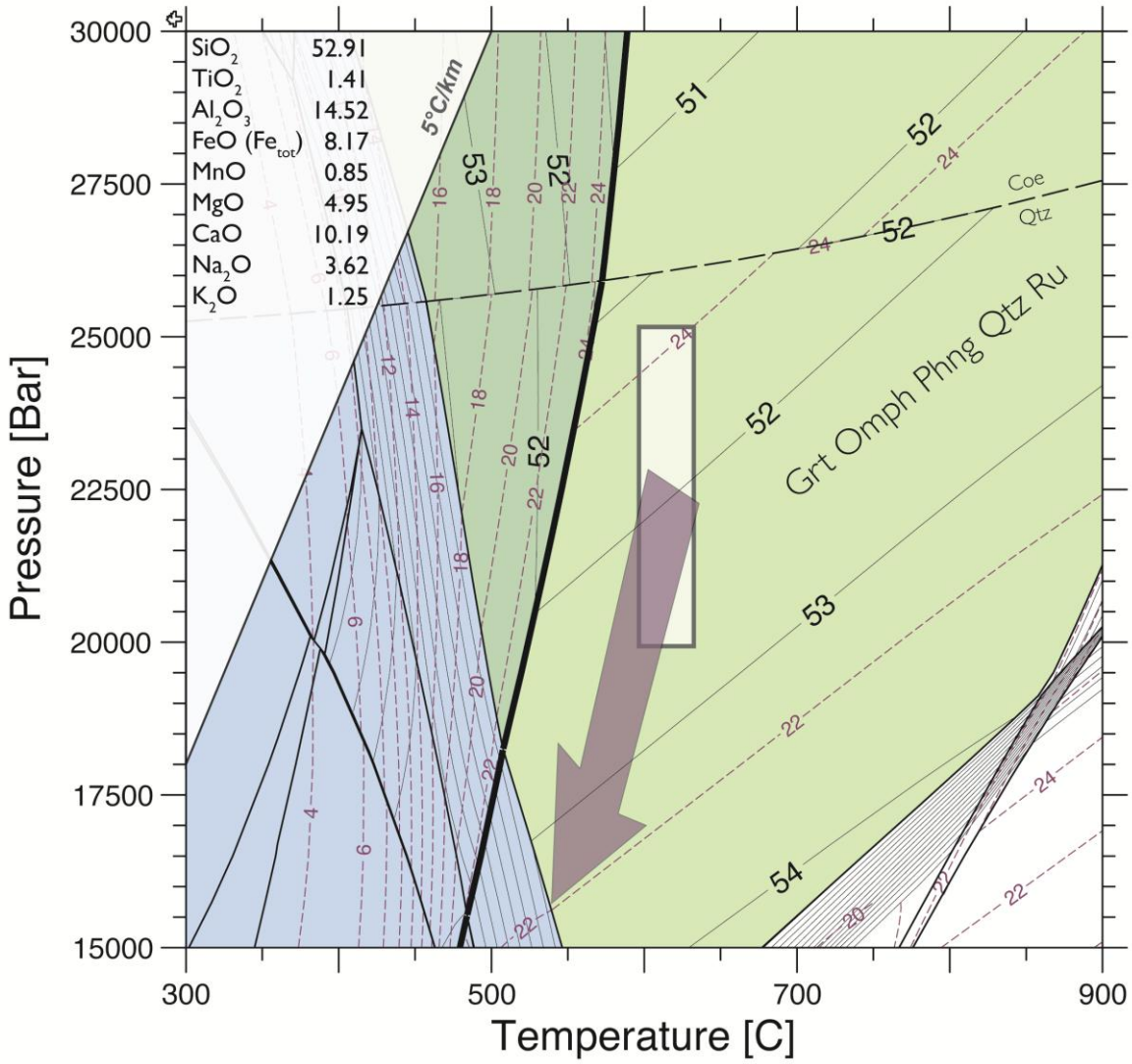

Figure 10

Highlights

- Analysis of crystallographic preferred orientations of high-pressure polymineralic rocks by time-of-flight neutron diffraction

- Elastic properties of a complete set of subduction channel rocks calculated from their crystallographic preferred orientation

- Vp/Vs ratio and P-wave anisotropy of eclogites and metasediments

- Influence of eclogite retrogression during exhumation on their elastic properties

- Evaluation of the seismic signature of both clastic and carbonate sediments in subduction channels